Non-Equilibrium Dynamics of Biological Matter in Microfluidic Environments - from Red Blood Cell Flickering to Conformational Transitions of Actin Filaments

Inauguraldissertation

zur

Erlangung der Würde eines Doktors der Philosophie

vorgelegt der

Philosophisch-Naturwissenschaftlichen Fakultät

der Universität Basel

von

Michael Göllner

aus

Augsburg, Deutschland

Basel, 2017

Originaldokument gespeichert auf dem Dokumentenserver der Universität Basel

edoc.unibas.ch

Genehmigt von der Philosophisch-Naturwissenschaftlichen Fakultät
auf Antrag von

Prof. Dr. Wolfgang Meier, Dr. Thomas Pfohl und Prof. Dr. Cornelia Palivan

Basel, den 21.03.2017

Prof. Dr. Martin Spiess

Abstract

Even the most basic and seemingly simple living biological systems exist far from thermodynamic equilibrium and studying their dynamic behavior represents a crucial step towards a better understanding of their fundamental properties. Here, we present the investigations of two different, out-of-equilibrium biological systems, namely single cell studies on the human red blood cell (RBC) and single macromolecule analysis of actin filaments, both by exploiting the exceptional physics at the micro-scale and the corresponding unique capabilities of experimental control.

In particular, existing approaches to RBC analysis on the single-cell level usually rely on chemical or physical manipulations that often cause difficulties with preserving the RBC's integrity in a controlled microenvironment. We introduce a straightforward, self-filling microfluidic device that autonomously separates and isolates single RBCs directly from unprocessed human blood samples and confines them in diffusion-controlled microchambers by solely exploiting their unique intrinsic properties. Using bright-field microscopy, this noninvasive approach enables the time-resolved analysis of RBC flickering during the reversible shape evolution from the discocyte to the echinocyte morphology. A better understanding of this central shape transformation is especially relevant for blood storage applications as the formation of echinocytes can affect blood handling. We are further able to study the photo-induced oxygenation cycle of single functional RBCs by Raman microscopy without the limitations typically observed in optical tweezers based methods. Due to its specialized geometry, our device is particularly suited for studies on single RBCs under precise control of their environment. The provision of important insights into the RBC's biomedical and biophysical

properties will improve the understanding of RBC microcirculation and can further contribute to advances in pathology diagnosis.

Furthermore, we study the non-equilibrium conformational dynamics of semiflexible actin filaments experiencing hydrodynamic forces. Improving the knowledge about these dynamic processes of semiflexible polymers is of particular importance for the description of unusual transport in cellular flows and pattern formation processes in cytoplasmic streaming. The actin filaments are flowing through structured microchannels with alternating high- and low-velocity segments. These flow fields of spatially varying flow strength result in a compressive force on the filaments when they are entering the low-velocity regions and conversely an extensional force is acting on them when they are reentering the high-velocity segments. The semiflexible actin filaments undergo a length-dependent buckling transition under compression with a corresponding change in end-to-end distance and a rise in bending energy. However, the degree of increase of the length-normalized bending energy shows no evident dependence on the contour length. Increasing the fluid flow velocity results in a large rise of the compressive hydrodynamic force with a strong increase in storage of elastic energy due to the bending of the semiflexible filaments. At the passage from the low-velocity segments to the high-velocity ones, an extensional force is acting on the partially elastically relaxed filaments and a conformational transition from a coiled to a stretched state with a suppression of thermal fluctuations can be observed. Despite the symmetry of the microfluidic channels and therefore a similar rate of the absolute values of extension or compression in the specific channel segments, the observed stretch-coil and coil-stretch transitions distinctly differ in the evolution of the conformational changes and bending energies. This asymmetry of the non-equilibrium and non-stationary conformational transitions shows a strong dependence on the contour and persistence length, the degree of relaxation and the extensional or compressional rate. Many polymer solutions are non-Newtonian fluids and our studies may therefore have an impact on the analysis as well as sorting of polymers by elucidating the non-Newtonian flow behavior of semiflexible filaments in specific microflows, which may consequently lead to a better understanding of intercellular flows.

Contents

The following chapters contain extracts from recent publications by the thesis author:

Chapter 2 - 4 & 6

M. Göllner, A. C. Toma, N. Strelnikova, S. Deshpande and T. Pfohl. A self-filling microfluidic device for noninvasive and time-resolved single red blood cell experiments. *Biomicrofluidics* **10**, 054121 (2016) [1]

Chapter 5 & 6

N. Strelnikova*, M.Göllner* and T. Pfohl. Direct observation of alternating stretch-coil and coil-stretch transitions of semiflexible polymers in microstructured flow. *Macromolecular Chemistry and Physics* **218**, 1600474 (2017) *contributed equally [2]

Chapter 1

Biophysics and the Grammar of Science

In the early 19th century, the prevailing notion was that living organisms depend on special biological laws and that the corresponding forces differ from those that define the inorganic world. In contrast, a group known as the Berlin school of physiologists including pioneers such as Carl F. W. Ludwig, Johannes Peter Müller, Ernst Heinrich Weber and Hermann von Helmholtz [3] strove to explain biological function by using the same laws as can be applied in the case of chemical and physical sciences [4]. Although the group conducted some of their early studies already in the 1840s [5], the first published use of the word "Biophysics" was in Karl Pearson's book "The Grammar of Science" from 1892 [6]. Besides covering several general topics like the scope and methods of science, he pointed out that a branch of science is necessary that links physics and biology by dealing with the applications of the laws of inorganic phenomena. He then proposed that this new branch of science be called biophysics and that it "does not appear to have advanced very far at present, but it not improbably has an important future" [4, 6]. The popularity of the field rose especially after the publication of the famous book "What is Life? The Physical Aspect of the Living Cell" by Erwin Schrödinger - a physicist. [7]. This interest in the physics of biological systems is undiminished ever since and scientists are beginning to fulfill the vision of their colleagues from almost 200 years ago.

Despite biophysics being such a thriving discipline, biophysicists often find themselves challenged when they are asked to describe what the term actually represents [4]. Especially the overall mindset how to approach the study of biological systems often differs significantly between scientists. In general, the nature of biophysics should be defined by the quantitative study of biological systems and their phenomena, i.e., by scientific problems and the corresponding approaches. However, the motivation should not be based on the application of a specific method for the sake of the method itself but instead being founded on the curiosity to study the physics behind biological structures, organization and functions.

In this thesis, two different biological systems are investigated and the motivation of their analysis is based on their unique structure, function and behavior in dynamic environments. In particular, even the most basic and seemingly simple living biological systems are not in thermodynamic equilibrium but are either changing or can be triggered to change over time by being subjected to flux of matter and energy as well as to chemical reactions. Interacting components are therefore changing with time in response to external and internal events and these so-called non-equilibrium dynamics are the rule rather than the exception as biological systems exhibit rich dynamic behavior over a vast range of time and length scales [8]. This implies a shift from a static to a dynamic view and the corresponding understanding how properties of the system emerge from nonlinear interactions with its environment. These principles build the foundation for the phenomenon-motivated methodological developments presented in this thesis by means of exploiting and not justifying the applied experimental techniques and methods of analysis in order to study single cell and single macromolecule dynamics.

More specifically, the first part (chapter 2 - 4) of the dissertation addresses the development, characterization and application of a microfluidic device that presents a straightforward and elegant approach to dynamic single red blood cell (RBC) experiments. The second part (chapter 5) describes the analysis of conformational transitions of actin filaments in microstructured flow based on provided experimental data. In both parts of the thesis, image processing algorithms are custom-developed as a means for the purpose of

analyzing the non-equilibrium dynamics of the presented biological systems.

Chapter 2 introduces the remarkable properties of the human RBC and highlights current experimental limitations. We further present a unique approach that overcomes these limitations based on the idea of exploiting RBC deformability and microscale physics to enable for precisely controlled as well as dynamic RBC experiments on the single cell level. The implementation of the microfluidic design through customized fabrication processes as well as materials is demonstrated and the fundamental attributes of our device are evaluated, like the capturing efficiency of single RBCs from unprocessed human blood samples and their motion inside the microfluidic system.

Based on their movement, chapter 3 explains the principles of membrane edge fluctuation analysis by decoupling the different types of RBC motion and demonstrates the feasibility of reversible and time-resolved single cell analysis. In particular, we analyze RBC membrane fluctuations in osmotic steady states and investigate the dynamics of RBC flickering during the reversible shape evolution from the discocyte to the echinocyte morphology.

The study of molecular processes within the RBC by the application of a custom-built confocal Raman microscope is presented in chapter 4. The basic principle of Raman scattering is introduced and the construction as well as the components of our custom-built setup are presented. We study the reversible photo-induced oxygenation cycle of single functional RBCs by resonance Raman spectroscopy and further highlight the advantages to currently available methods.

Chapter 5 investigates the conformational dynamics of actin filaments flowing through spatially structured microchannels with alternating high- and low-velocity segments. Actin is introduced as a model system for fibrous biopolymers and the features of the microfluidic system that enables the study of non-equilibrium conformational dynamics of semiflexible actin filaments are discussed. We show that the flow fields of spatially varying flow strength lead to the observation of fascinating non-equilibrium conformations due to hydrodynamic forces acting on the filaments. The nature of these transitions are characterized by analyzing the evolution of the end-to-end distances, center-of-mass velocities and bending energies along the course

of the filaments through the microchannels. In particular, the dependence of contour length, fluid flow velocity and channel segment aspect ratio on the filament's conformational transitions are investigated.

Chapter 6 represents a conclusion by summarizing the main achievements and results as well as briefly giving an outlook towards possible future directions, developments and applications.

Chapter 2

The Elegance of Simplicity - About a Unique Approach to Single RBC Experiments[†]

2.1 Remarkable Properties of the RBC and Current Experimental Limitations

Containing a wealth of information, human blood is still one of the most common used samples for diagnostic purposes [9]. In particular, the red blood cell (RBC) is the most abundant cell type in the human body comprising approximately 70 % of the total cell number with a continuous production rate in the bone marrow of about 2.4 millions per second [10,11]. The composition of a whole human blood suspension additionally illustrates the intrinsic importance of the RBC by physiologically containing 40 to 45 % RBCs by blood volume and more than 99 % by blood cell quantity [12] (Fig. 2.1a). During its 115 days of mean lifespan, the RBC is completing about $5 \cdot 10^5$ cycles of circulation through the human body and constitutes the principle means of delivering oxygen to tissues [13].

The anucleate RBC is unique among human cell types as it presents a remarkable capability to undergo large passive deformations in order to tra-

[†]This chapter is partially reprinted and modified from Ref. [1].

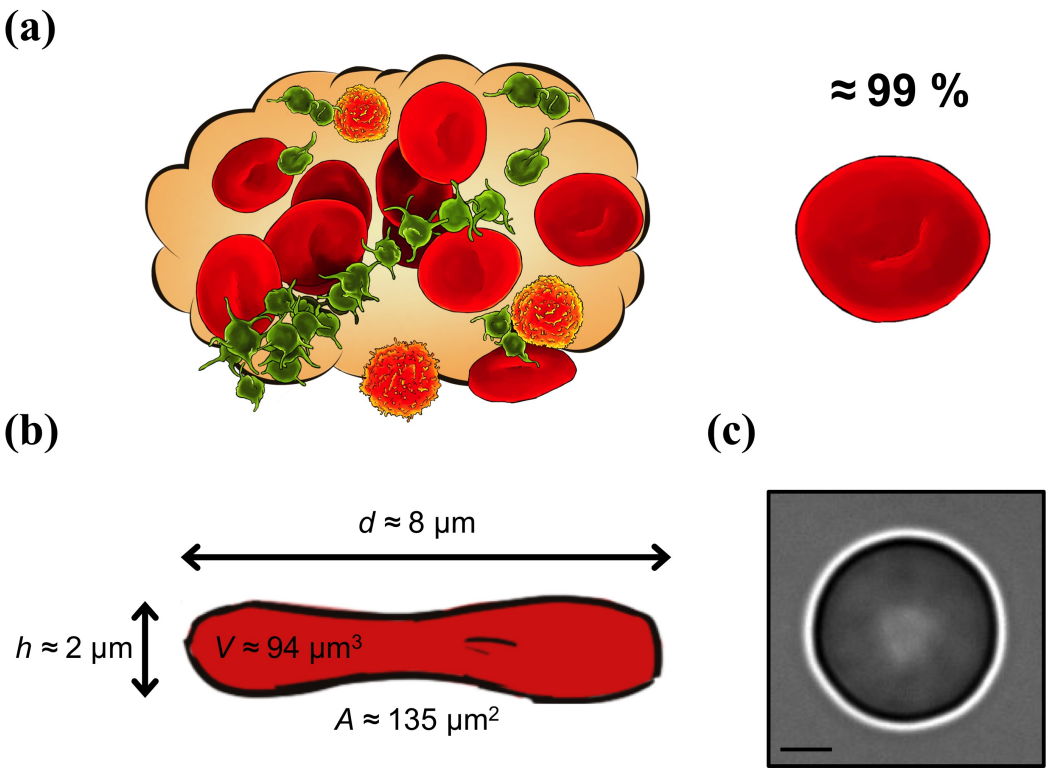

Figure 2.1: The human red blood cell. (a) The RBC is the most prevalent type of blood cell with about 99 % RBCs by cell quantity in unprocessed human blood. (b) Biconcave discoid morphology of the RBC under physiological conditions. (c) Brightfield microscopy image of a typical RBC discocyte. Scale bar: 2 µm.

verse splenic cords and narrow micro-capillaries with cross-sections as small as one-third of its own diameter [14]. Consequently, reduced RBC deformability is considered as one of the direct causes of increased RBC clearance in the spleen, leading to a crucial connection between its mechanical properties and the main filtering process of blood in the human body [15]. The extraordinary deformability of healthy RBCs is the combined result of the surface area-to-volume ratio, the viscosity determined by the hemoglobin (Hb) content and the elastic properties of the membrane-cytoskeleton complex [16]. Especially the latter have attracted increasing attention since the first observation of the vibratory motions of the RBC's plasma membrane by optical microscopy

during the nineteenth century [17]. This so-called 'flickering' of the membrane has been related to its biomechanical properties which have been studied extensively both in single-cell experiments as well as theoretical work [18–22]. However, one of the fundamental questions regarding RBCs that still remains controversial is whether these membrane fluctuations are driven by an active process or are simply thermal motion [22]. Flickering analysis additionally shows promising potential for malaria diagnosis [23] as membrane-related RBC abnormalities represent both a cause of and a biomarker for diseases [14, 24]. Moreover, adhesive phenomena such as rouleau formation may also be controlled by membrane fluctuations as it has been suggested that one of the important biological functions of flickering is the decrease of interactions between RBCs [20, 25].

Furthermore, the overall morphology of the human RBC plays a crucial role in the determination of their microcirculatory deformability as well and represents another diagnostic indicator that is encoded in the mechanical properties of the cell membrane. When not subjected to external stress and under physiological conditions, healthy human RBCs assume a distinctive biconcave discoid geometry, the well-known discocyte (Fig. 2.1b,c) [26]. Here, a concentrated intracellular Hb solution is surrounded by a viscoelastic membrane which forms the only structural component of the RBC [14]. Mechanically stable shapes of the RBC are assumed to represent energy minima of the plasma membrane under the constraint of a fixed surface area and cell volume [27]. Based on this model, several theoretical studies predicted the morphological transition from the normal discocyte to a series of crenated echinocyte shapes that appear under certain conditions like increasing salt concentration [27–29].

However, although these morphologies and RBC flickering are known since decades, available experimental approaches to the analysis of single RBCs in general, as well as to RBC flickering and shape analysis in particular, are lacking a precise control over the cell's microenvironment [18–22]. Single RBC analysis is therefore currently limited to steady state measurements without the feasibility of investigating the temporal behavior of RBCs exposed to an external stimulus, e.g., studying the dynamics of the disco-

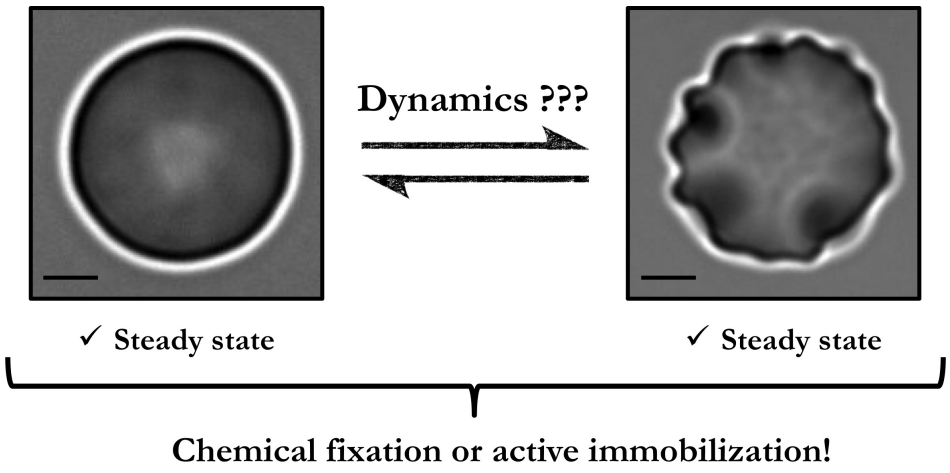

Figure 2.2: Reversible diso-echinocyte transition of the human RBC exemplifies the general limitation of current experimental approaches to RBC steady state analysis, i.e., lacking the feasibility of investigating the dynamics of functional RBCs exposed to external stimuli. Scale bars: 2 µm.

echinocyte transition and *vice versa* (Fig. 2.2). Moreover, the techniques that enable single-cell experiments by separating and isolating individual cells from the bulk often include rather complicated manipulations that further cause difficulties with preserving the RBC's integrity. These procedures include methanol fixation [30] or adsorbing the cells onto poly-lysine covered glass surfaces which might lead to adsorption-dependent changes of the cell's intrinsic properties [31]. Alternative methods use active immobilization of single RBCs by optical tweezers in order to avoid adsorption-induced effects due to chemical fixation. However, the required high-intensity trapping lasers can already induce hemolysis [22] and the stress levels introduced on the RBC often represent the limiting factor in acquiring information of which the experiment is actually aiming for [32].

2.2 Microfluidic Design - Exploiting RBC Deformability and Microscale Physics

Making the simple complicated is commonplace. Making the complicated simple, awesomely simple, that's creativity. (Charles Mingus)

All approaches to single cell experiments are based on the same principle, the combination of a method to separate and isolate single cells from the bulk with a technique to extract the relevant biological or biophysical information [33, 34]. However, state-of-the-art experimental techniques lack the ideal combination of a principle that enables separation and isolation which is easy to implement, the application of minimal stress on the cell during the whole experimental procedure, avoiding interference with the RBC's physiological processes as well as offering precise control over its environment.

We present an elegant and straightforward approach to RBC experiments on the single cell level that complies these requirements by combining the intrinsic properties of the RBC itself with reductionism as the foundation of single cell analysis: a specific microfluidic design that solely exploits the remarkable deformation capability of the RBC and the unique physics at the microscale.

The main characteristics of our method involve the direct application of unprocessed human blood samples on an empty microfluidic device (Fig. 2.3a), its self-filling purely driven by capillarity and the separation of individual RBCs from the undiluted bulk into a precisely controlled microenvironment (Fig. 2.3b). These particular features are implemented by a specific multi-height microfluidic geometry with dimensions of the connections (cross-section: $2\,\mu m \times 2\,\mu m^2$, length: $10\,\mu m$) between a controlling channel (width: $50\,\mu m$, height: $10\,\mu m$) and microchambers (area: $100\,\mu m \times 100\,\mu m^2$, height: $2\,\mu m$) that are in the size range of the smallest human capillaries in order to minimize the probability of RBCs entering the chambers. Consequently, as unprocessed blood is flowing through the initially empty device driven by capillary forces, separation as well as isolation of individual RBCs from the bulk into a single cell environment is achieved autonomously and is based on

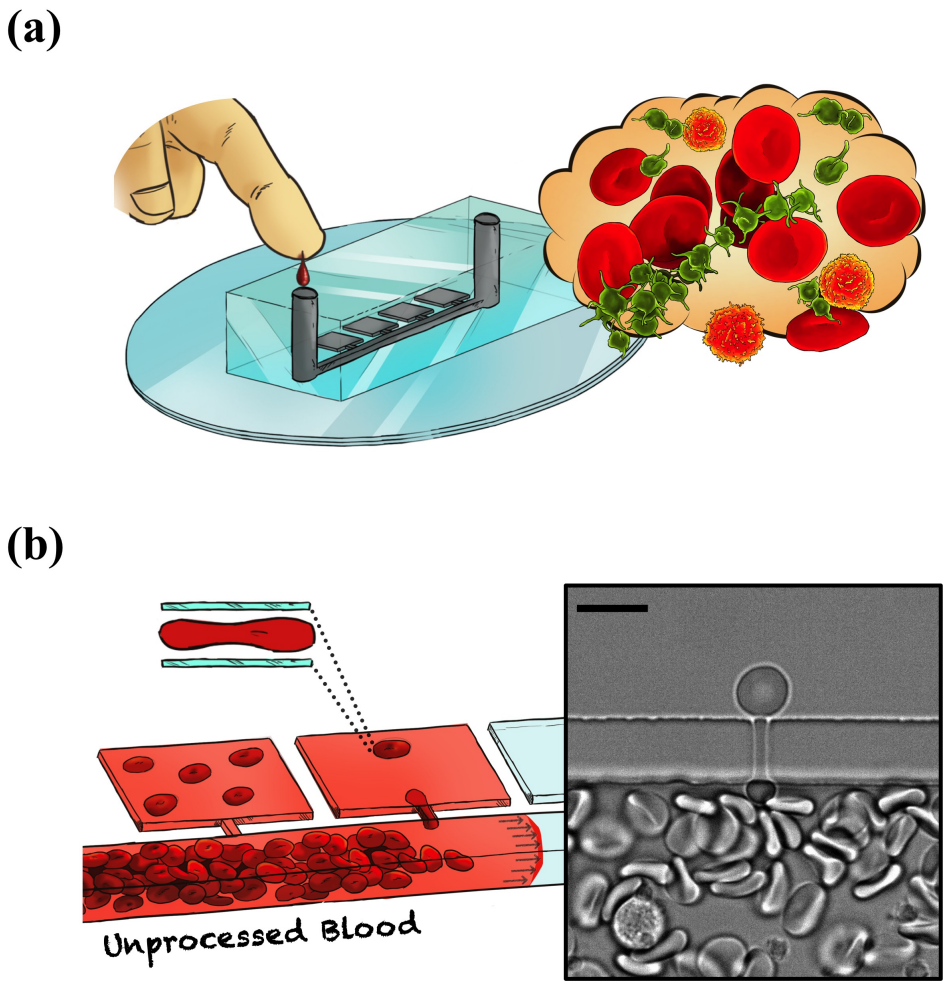

Figure 2.3: Design and operation of the blood chip for noninvasive and versatile single RBC analysis. (a) Unprocessed human blood can be directly applied on the empty microfluidic device and its initial filling is purely driven by capillarity. (b) Single RBCs are passively separated by capillary forces from the high cell density bulk through narrow connections between the controlling channel and low-height microchambers. Individual RBCs are further placed horizontally inside the chambers and are only confined with respect to motions out of the image plane, offering ideal conditions for versatile microscopic or spectroscopic studies on single functional RBCs. Scale bar: 10 µm. Reprinted and modified from Ref. [1].

the intrinsic mechanical properties of the RBC itself, without any chemical or active physical manipulations. Due to the low height of the chambers, the RBCs are further placed horizontally inside them and are only confined with respect to motions out of the image plane, creating ideal conditions for ver-

satile microscopic or spectroscopic studies of functional RBCs on the single cell level.

Microfluidics can be essentially described as the science and technology of systems that is dedicated to the behavior, precise control and manipulation of small amounts of fluids ranging from 10^{-9} L to 10^{-18} L by using geometrical constraints with dimensions of one to hundreds of micrometers [35]. One direct consequence of miniaturization is the dramatic reduction in sample and reagent volumes by a factor of 10^9 (e.g., from L to nL) when the characteristic dimension of a fluidic system is downscaled by three orders of magnitude (e.g., from 1 dm to 100 µm). Apart from this practical benefit of our approach through applying microfluidics to single RBC analysis, fluids at the microscale further show very interesting and less familiar physical properties that are substantially different from the behavior of fluids from the world we have developed our intuitions in [36]. As a result, microfluidics not only exploits the obvious advantage of very small blood sample volumes, but more importantly, the unintuitive phenomena occurring on the nanoliter scale and therefore offers fundamentally new capabilities of experimental control [35]. Decreasing the physical length scale of a fluidic system to the microscale generally increases the relative influence of forces due to viscous friction and surface tension with respect to forces resulting from inertia and gravitation [37]. This represents a major difference compared to macroscale flows and directly leads to the crucial advantage of diffusion-controlled mixing in microfluidic systems as flow becomes laminar rather than turbulent [38]. Besides the possibility to precisely control the concentration of molecules in space and time by diffusion, the shift of balance between forces is additionally leading to several practical advantages, like the possibility of filling up a microchannel by capillarity, which would be unthinkable in a macroscopic device [39].

The unique characteristic of laminar flow in microfluidic devices is the direct result of a reduced relative importance of inertia to viscous dissipation and the ratio of the corresponding forces for given flow conditions is defined by the dimensionless Reynolds number [40] (Fig. 2.4a),

$$Re \equiv \frac{\text{inertial forces}}{\text{viscous forces}} = \frac{av\rho}{\eta} = \frac{av}{\nu} \tag{2.1}$$

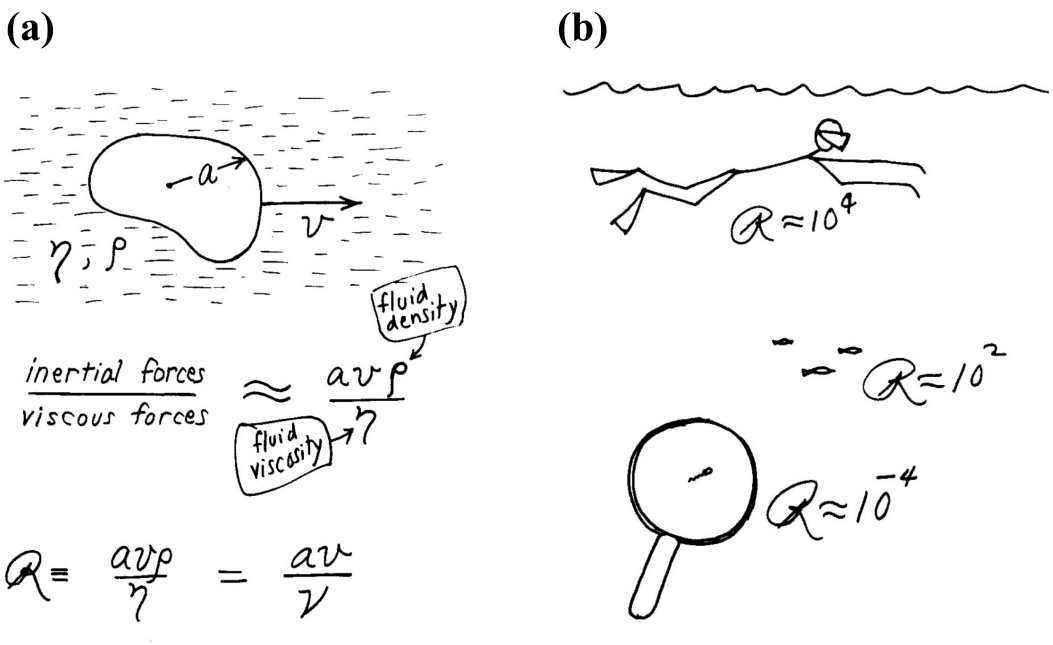

Figure 2.4: Life at low Reynolds number. (a) The Reynolds number is an important dimensionless quantity in fluid mechanics and describes the balance between inertial and viscous forces. (b) For a "macroscopic swimmer" like a human or a fish, the inertial forces dominate over the viscous forces. Conversely, inertia is totally irrelevant for swimmers at the microscale and therefore result in a corresponding low Reynolds number. Reprinted and modified from Ref. [36].

were ρ is the density and η the dynamic viscosity of the fluid, ν the kinematic viscosity, v is the flow velocity and a the characteristic length scale of the channel. Reynolds numbers for microfluidic systems are low (Fig. 2.4b) and in the range of 10^{-6} to 10, assuming water as the typical applied fluid, 1 µm/s - 1 cm/s as common flow velocities and 1 µm - 100 µm as typical channel dimensions [41].

After the initial filling of the device by capillarity, washing of the controlling channel with buffers is actively regulated by advection and due to the microfluidic nature of the blood chip, the flow in the controlling channel is laminar. Furthermore, material transport into the filled microchambers and *vice versa* is precisely controlled by diffusion, resulting from the multi-height design in addition to much smaller dimensions of the connecting channels

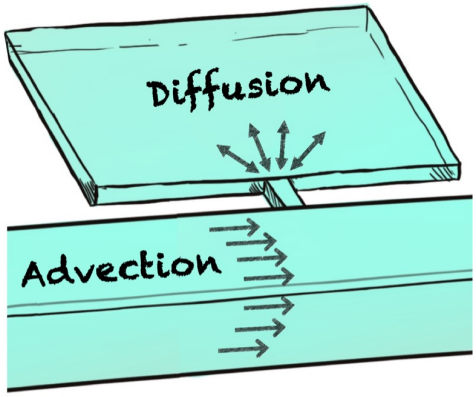

Figure 2.5: Precise control over the microenvironment of confined single RBCs. After initial filling of the device, flushing of the controlling channel is dominated by advection. The multi-height design in combination with much smaller dimensions of the connecting channels compared to the controlling channel results in diffusion-controlled material transport into flow-free microchambers and *vice versa*. Reprinted and modified from Ref. [1].

compared to the controlling channel (Fig. 2.5) [42–44]. The concentration of an added or depleted biochemical reagent inside the flow-free chambers is therefore directly related to the diffusion time t that has elapsed since the onset of an exchange buffer at the corresponding connecting channel. Variation of the RBC's microenvironment inside the flow-free chambers is further highly controlled and repeatable through diffusive washing with different buffer solutions via the controlling channel. As a result, our approach can serve as a general system to study the temporal behavior of single RBCs exposed to external stimuli, e.g., experimentally investigating the dynamics during the reversible shape evolution of non-adherent RBCs from the discocyte to the echinocyte morphology under altering osmolarity (Fig. 2.6). Here, a change of salt concentration inside the chambers is given by

$$c\left(x,y,t\right) = \frac{c_0}{4\pi Dt} e^{-\left(x^2+y^2\right)/4Dt} \tag{2.2}$$

where x and y are the coordinates of the RBC's center of mass, c_0 is the NaCl concentration of the buffer in the controlling channel and $D = 1.473 \cdot$

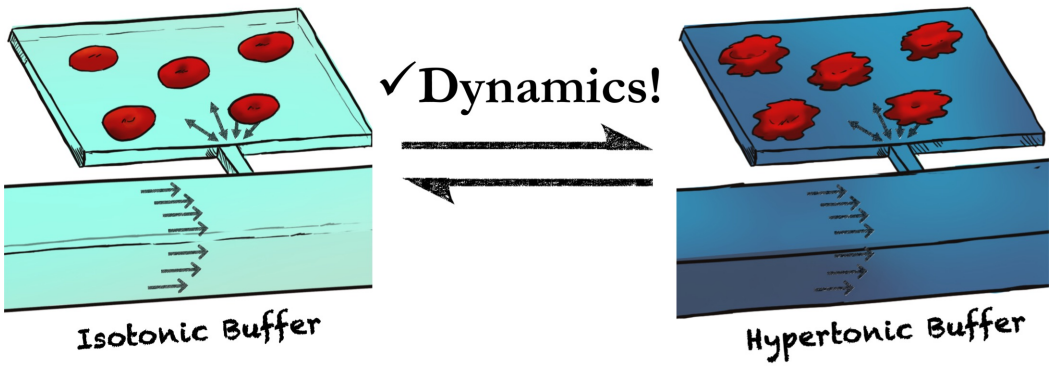

Figure 2.6: Precise and reversible control over the RBC's microenvironment enables the quantification of the temporal behavior of single RBCs exposed to an external stimulus, e.g., increasing the osmolarity by diffusive washing of the microchambers with hypertonic buffer through the controlling channel. Reprinted and modified from Ref. [1].

$10^{-9}\,\mathrm{m}^2/\mathrm{s}$ is the diffusion coefficient of NaCl [45]. The osmolarity can be calculated by $\Pi(x,y,t) = \varphi \cdot n \cdot c(x,y,t)$, where $\varphi = 0.921$ is the osmotic coefficient of NaCl [46] and $n = 2$ the number of ions into which NaCl dissociates.

2.3 From Design to Implementation - Realizing the Specific Device Features

The unique features of our microfluidic device for RBC analysis on the single cell level are realized by means of soft lithography, which can be viewed as a complementary extension of photolithography and encompasses a collection of fabrication methods that provides access to inexpensive as well as experimentally convenient three-dimensional structures [47]. Here, "soft" refers to the fabrication of an elastomeric replica from a rigid mold master that defines a stamp pattern and is typically produced by conventional photolithography. Although soft lithography can process a wide range of materials, polydimethylsiloxane (PDMS) has been the most widely used stamp resin for microfluidic applications due to its attractive properties [48, 49] including low cost, biocompatibility, gas permeability, low toxicity, chemical inertness, versatile surface chemistry and commercial availability. Furthermore, PDMS is transparent from the near ultraviolet to the near infrared, sealing of the replica can be achieved by oxidizing its surface requiring no adhesives and fabricating PDMS devices necessitates only few equipment.

In order to produce multi-height masters for further device fabrication, the microfluidic design is patterned on a clean silicon wafer (Si-Mat, Kaufering, Germany) by means of multi-layer photolithography (Fig. 2.7). In particular, the latter is baked at 200°C for 10 min on a hotplate to remove any remaining moisture on the surface that would reduce adhesion. Suitable negative photoresist (SU8-2002, MicroChem, Newton, USA) is applied by spin-coating (3000 rpm, 30 s) to create the first layer with a height of $h = 2\,\mu\text{m}$. The wafer containing the SU-8 film is baked at 95°C for 1 min in order to remove residual solvent from the resist as well as to stabilize the film. This pre-exposure bake further creates a non-sticking surface and therefore prevents the wafer from attaching to the mask, which is crucial for later alignment. The microfluidic design of the first layer is patterned on the wafer by cross-linking the photoresist through exposing certain areas to UV light (365 nm, 33 mW/cm^2, 3 s) by means of an appropriate chrome mask (ML&C GmbH, Jena, Germany) using a MJB4 mask aligner (soft contact mode, SUSS MicroTec AG, Garch-

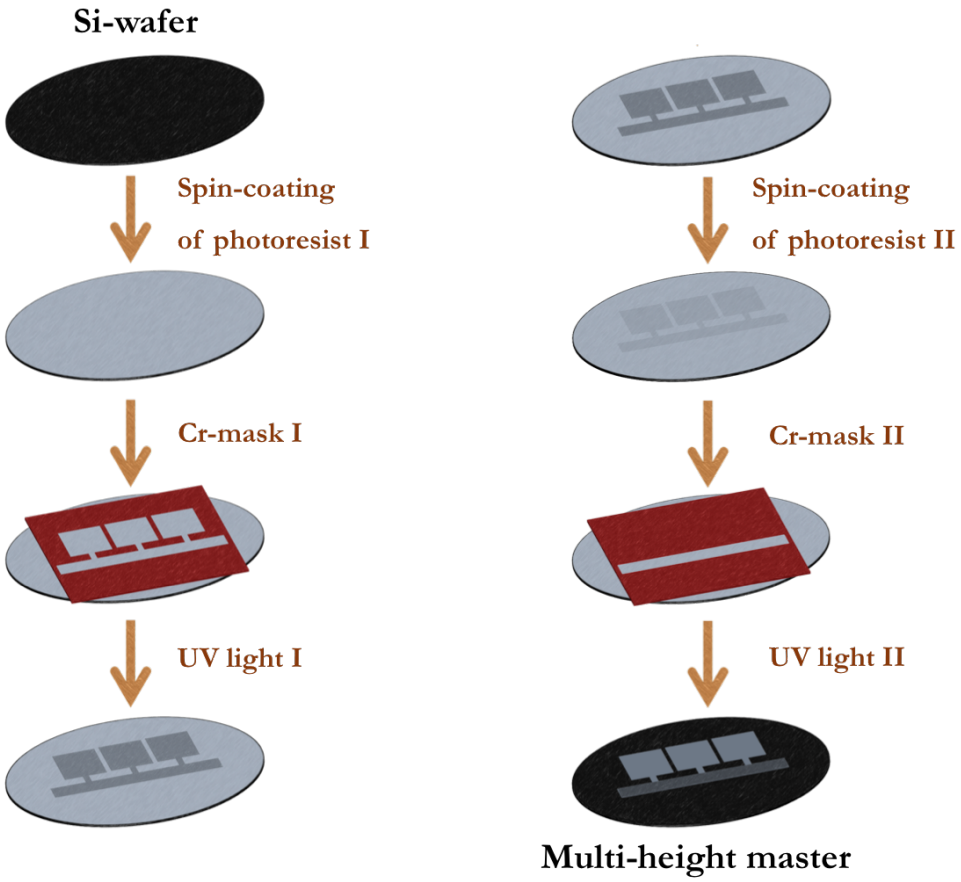

Figure 2.7: Multi-layer photolithography represents the first step in the fabrication of the microfluidic devices by creating a multi-height master that defines a stamp pattern of the specific geometry.

ing, Germany). Baking of the exposed wafer at 95°C for 2 min completes the polymerization process before spin-coating (4000 rpm, 30 s, $h = 8\,\mu m$) a second layer of photoresist (SU8-3005, MicroChem, Newton, USA) on the structure. Further soft-baking of the wafer at 95°C for 4 min as well as precise alignment with the matching chrome mask before a second exposure to UV light (5 s, hard contact mode), post-exposure bake at 95°C for 2 min and development with SU-8 developer results in the final multi-height master.

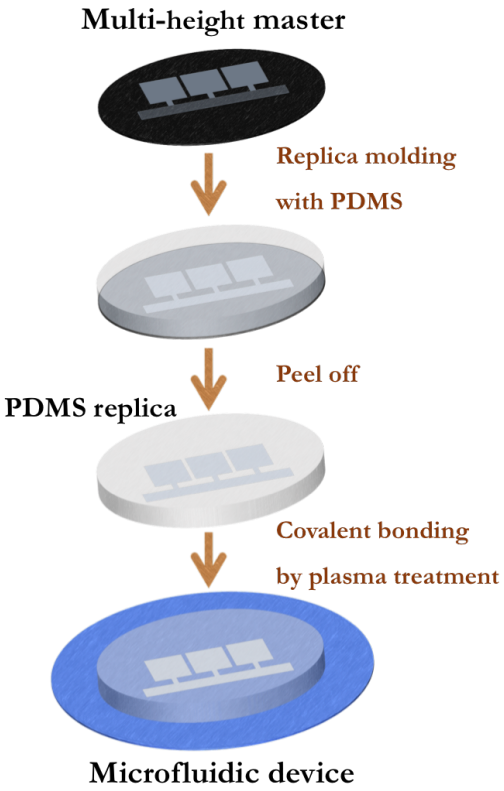

Figure 2.8: After production of the master, elastomeric PDMS replica molding and its sealing to a cover glass slide results in the final microfluidic device.

After production of the rigid master, microfluidic devices are fabricated by PDMS replica molding and subsequent sealing with a glass slide (Fig. 2.8). PDMS prepolymer and cross-linker (Sylgard 184, Dow Corning GmBH, Wiesbaden, Germany) are mixed at a 10:1 ratio, degassed in vacuum and cured at 80°C for 24 h. The cured elastomeric replica is peeled off from the master and holes of the inlets are punched with a multipurpose sampling tool (Harris Unicore, diameter 0.75 mm) in order to connect tubings (polytetrafluoroethylene (PTFE) microtube, outer diameter 1.07 mm) if necessary. As a result, replica molding leads to a patterned layer of PDMS where the microfluidic design is imprinted in the surface of the polymer. Microfluidic channels are formed by placing the PDMS replica on top of a glass surface that forms the floor of the device. However, channels formed by simple contact represent a

weak physical seal between the two layers of material, which is the reason why the PDMS stamp is covalently bound to the glass surface resulting in the possibility of pumping fluids through the device at pressures as high as 80 psi without failure [50]. The surface of PDMS is hydrophobic as it contains repeating units of -O-Si-$(CH_3)_2$-groups, but it can be rendered hydrophilic by exposure for 30 s to air plasma (Harris Plasma, NY, USA) in order to generate reactive silanol groups (Si-OH) at the surface [51]. An irreversible seal of the microfluidic device is achieved by bringing the freshly oxidized PDMS replica into contact with an oxidized cover glass in order to form irreversible Si-O-Si bonds between the layers of material by condensation reactions [52].

However, hydrophilic PDMS surfaces that are not bound to the cover glass and therefore constitute the microfluidic design are unstable and recover their hydrophobicity in less than an hour [53], due to low molecular weight chains diffusing from the bulk to the surface [54,55]. Keeping plasma-treated PDMS in contact with water or polar organic solvents would create an indefinitely hydrophilic surface [56], but would also prohibit the initial filling of the empty device with unprocessed blood by capillarity as well as the autonomous separation of individual RBCs from the bulk into the microchambers. In order to realise these fundamental features of the device, the hydrophilicity of the activated PMDS surfaces is made more permanent through eliminating low molecular weight species from the bulk by thermal aging [57]. In particular, the cured PDMS replica is additionally placed onto a hotplate at 150°C for 30 minutes before covalent bonding to a glass slide after surface activation at 2 mbar for 30 s in air plasma. The fabricated devices are left at room temperature for at least 12 hours to a maximum of 36 hours before applying unprocessed blood samples on the inlet of the device.

2.4 Evaluation of Functional Attributes - Capturing Efficiency and RBC Motion

In order to quantify the efficiency of the self-filling process, human blood samples were freshly prepared before each experiment by finger pricking of a healthy donor and directly applied on the empty microfluidic devices without any sample preparation. Individual RBCs inside the microchambers were counted from brightfield microscopy images, acquired by an Olympus IX81 inverted microscope equipped with a 100x (N.A. 1.49) UApo N oil immersion objective (Olympus, Tokyo, Japan) and a complementary metal-oxide-semiconductor (CMOS) camera (pco.edge, PCO, Kelheim, Germany). The probability of chambers (area: $100\,\mu m \times 100\,\mu m^2$, height: $2\,\mu m$) containing at least one RBC is 93.6 %, with a mean RBC count inside the filled chambers of $\langle N \rangle_{RBCs} = 19.8 \pm 10.6$ (Fig. 2.9). Consequently, compared to whole blood in the controlling channel, the volume fraction of RBCs inside the chambers is reduced by a factor of four to five, with $\chi = \langle N \rangle_{RBCs} \cdot \langle V \rangle_{RBC} / V_{chamber} = (9.6 \pm 5.1)$ %, where $\langle V \rangle_{RBC} = 94\,fL$ is the average volume of a human RBC [26].

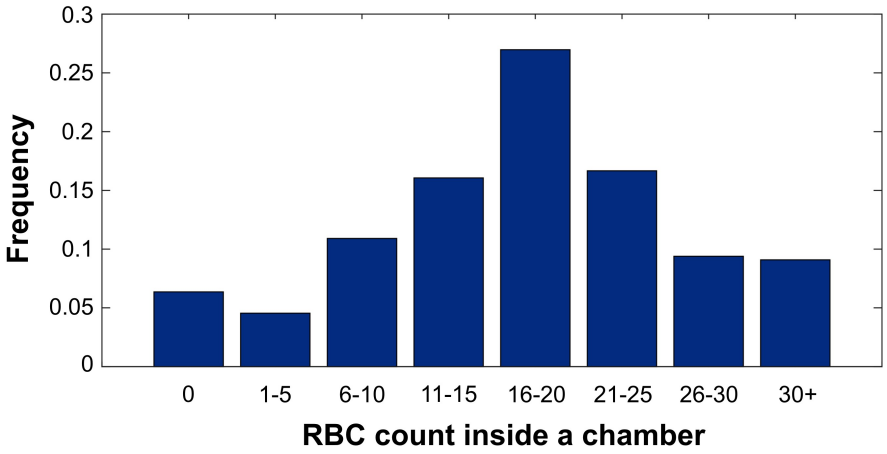

Figure 2.9: Distribution of RBCs autonomously captured into the microchambers.

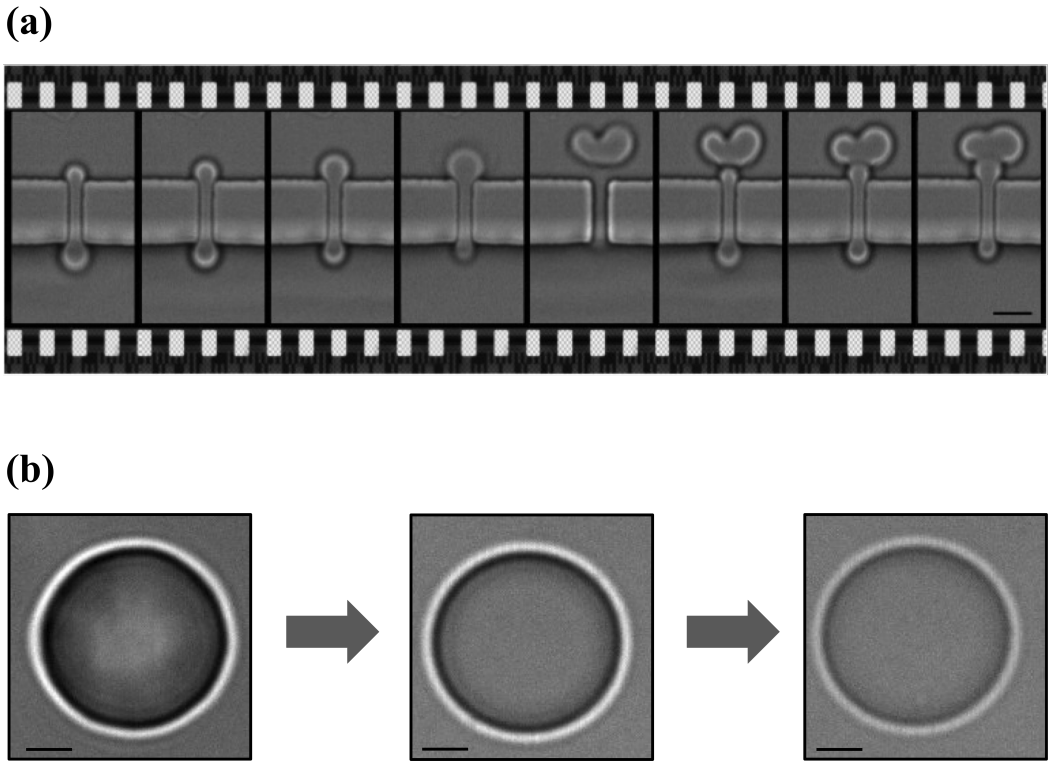

Figure 2.10: (a) RBCs undergo large deformations during the process of traversing the narrow connecting channels and entering through the microchambers purely driven by capillarity. Picture sequence from left to right, scale bar: 4 µm. (b) Evolution of bright-field microscopy images of a RBC during ghost formation. Here, the hemoglobin and other cytoplasmic components are washed out while still preserving the spectrin containing submembranous cytoskeleton, which results in a reduced image contrast of the RBC's outline. Scale bar: 2 µm.

During this autonomous filling and *in situ* dilution process, the RBCs have to traverse through the narrow connection channels with a cross-section that is much smaller than the cell's own diameter (Fig. 2.10a). In principle, hemolysis of individual RBCs can occur as a consequence of entering through these narrow connections to the chambers, resulting in so-called RBC ghosts [58]. The process of RBC ghost formation (Fig. 2.10b) can be observed by imaging the microchambers already during the initial filling process as well as during the first minutes afterwards. However, because of their naturally high deformability, the fraction of lysed RBCs inside the microchambers is only

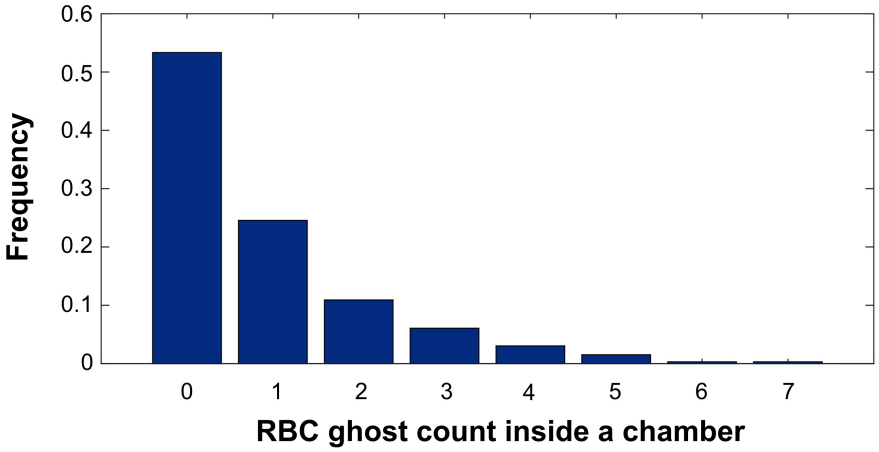

Figure 2.11: Distribution of RBC ghosts inside the microchambers clearly shows that the great majority of the captured RBCs remain functional while entering through the narrow connections between the controlling channel and the chambers.

4.8 % with 53.3 % of the chambers containing no RBC ghosts (Fig. 2.11). Furthermore, due to the RBC constituting by far the most frequent cell type in unprocessed human blood and additionally being unique with respect to its remarkable deformation capability, 97.6 % of the microchambers show no other type of blood cells than RBCs.

Although being confined with respect to movements out of the image plane, RBCs inside the chambers are still exhibiting 2D-translational (D_{xy}) and 1D-rotational motion around the z-axis (D_r, see chapter 3) in addition to their membrane edge fluctuations (δ, see chapter 3) (Fig. 2.12a). In order to investigate the translational motion of the confined RBCs, brightfield microscopy images are recorded at 900 fps and custom-built algorithms using MATLAB (version R2012b, The MathWorks, Natick, USA) are applied to identify the contour of the cells. Their center of mass movement is determined by averaging the smoothed coordinates of the pixel contour for each frame of the movie and the mean square displacement,

$$\mathrm{MSD} = \left\langle \left(r\left(t+\tau\right) - r\left(t\right) \right)^2 \right\rangle \tag{2.3}$$

where τ is the time interval, is calculated from the corresponding trajectories.

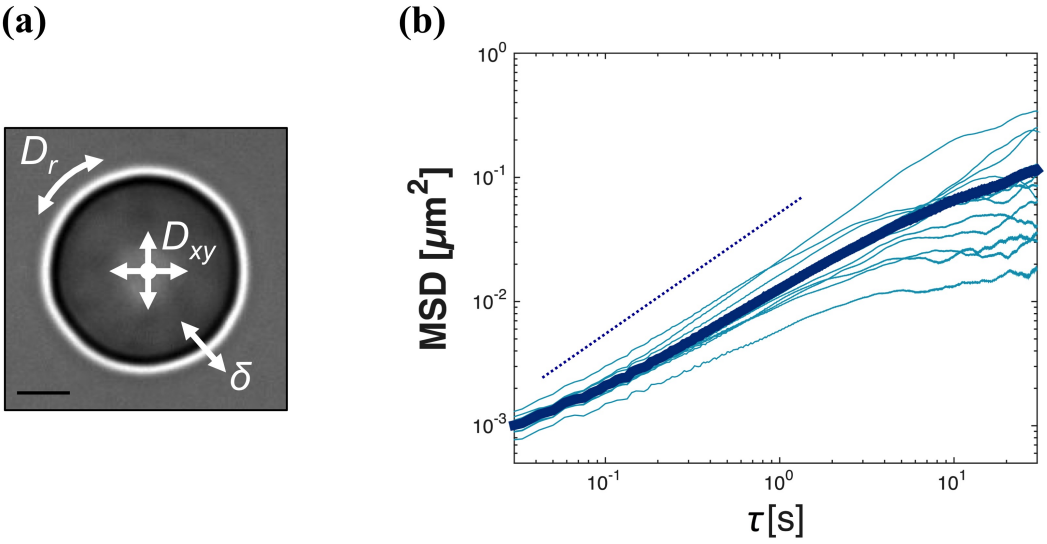

Figure 2.12: RBC motion. (a) The specific geometry of the microfluidic chambers conserves the RBC's 2D-translational motion in the image plane (D_{xy}) and around the z-Axis (D_r) in addition to their membrane edge fluctuations (δ). Scale bar: 2 µm. (b) Mean square displacement calculated from the center of mass of single RBCs inside microchambers under unprocessed blood conditions clearly indicates that their motion is diffusive with an absence of adhesive interaction. Reprinted and modified from Ref. [1].

In two dimensions, the time dependence of the MSD can be described by

$$\text{MSD} = 4 \cdot M_\alpha \cdot \tau^\alpha \tag{2.4}$$

where α is the scaling exponent and M_α the motility coefficient [59]. The motion is transported or super-diffusive for $\alpha > 1$, limited or sub-diffusive for $\alpha < 1$, and freely-diffusing or random walk-like for $\alpha = 1$ [59, 60]. The mean square displacement, calculated from the center of mass movement of single RBCs under unprocessed blood conditions shows the absence of adhesive interactions with a mean slope of $\alpha \approx 1$, indicating that their motion inside the microchambers is diffusive (Fig. 2.12b). For two-dimensional isotropic diffusion, the mean squared displacement is further given by MSD $= 4D_{xy}t$, resulting in a translational diffusion constant of $D_{xy} = (4.3 \pm 2.4) \cdot 10^{-3}$ µm^2/s for the RBCs inside the microchambers.

In summary, our unique and elegant approach to single RBC experiments is based on a self-filling microfluidic device for single RBC assays starting directly with unprocessed, small volume human blood samples. Our specific multi-height design solely exploits the remarkable deformation capability of the human RBC itself in order to autonomously separate and isolate single functional RBCs from the undiluted bulk into diffusion-controlled microchambers. The RBC density is largely reduced during this process, resulting in a single cell environment with mostly no interactions between cells. Furthermore, the great majority of the cells remain functional while entering the chambers and are still experiencing diffusive motion inside them. In particular, the RBCs are only confined horizontally within the microchambers, representing ideal conditions for versatile investigations on single RBCs without any chemical fixation and its corresponding adsorption-induced effects.

Chapter 3

Flickering Analysis Reveals the Dynamics of RBC Morphological Transformations[†]

3.1 Decoupling Membrane Fluctuations from Holistic RBC Motion

Offering precise control over the RBCs microenvironment, our approach is ideally suited to investigate RBC flickering not only in osmotic steady states but to overcome the limitations of available approaches by analyzing the dynamics of this fundamental RBC process during the morphological discocho-echinocyte transformation. Due to the diffusive motion of the non-adherent RBCs inside the microchambers, the description of membrane edge fluctuations is not feasible by means of standard correlation of their local contour lines and requires a translationally and rotationally invariant analysis of RBC flickering. In particular, we used custom-developed MATLAB scripts extending the commonly used radial Fourier analysis method for stationary particle shape characterization [61, 62] to our dynamic system in order to decouple global membrane edge fluctuations from the holistic motion of the RBC.

[†]This chapter is partially reprinted and modified from Ref. [1].

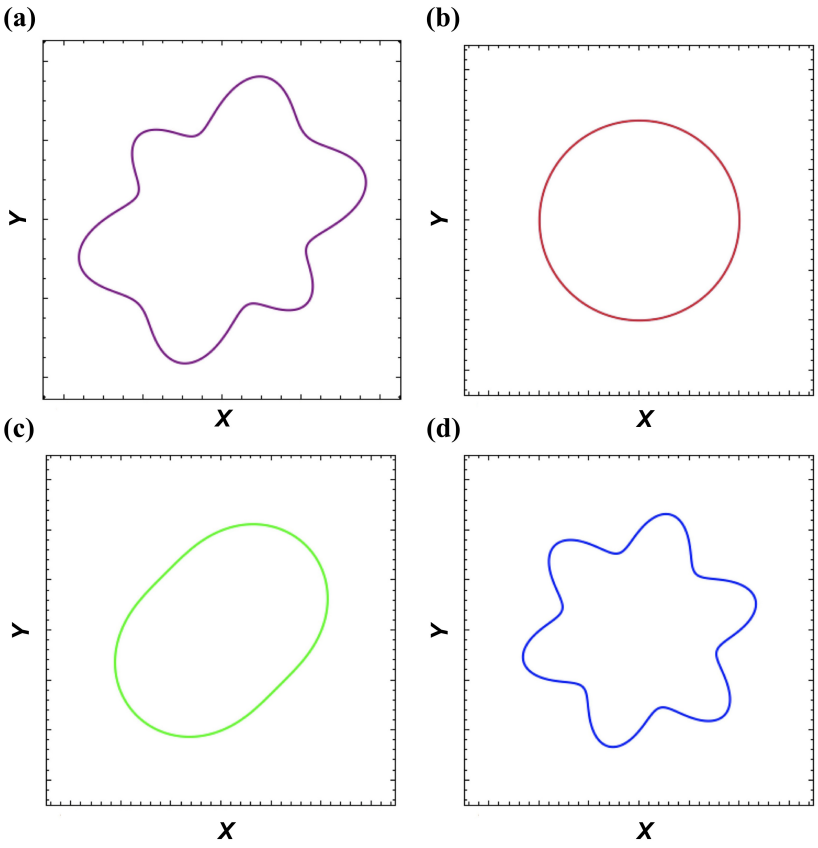

Figure 3.1: Principle of radial Fourier analysis for stationary particle shape characterization. The outline of a complicated two-dimensional shape (a) is decomposed into a set of simpler components (b - d) with specific individual contributions to the observed boundary outline. Reprinted and modified from Ref. [62].

Classic radial Fourier analysis is one of the oldest methods for boundary outline analysis and is based on the representation of any periodic function to a desired level of accuracy by a series of simple oscillating functions, namely sines and cosines. In terms of shape analysis, a complicated boundary curve in a Cartesian coordinate space is decomposed into a set of simple component curves (Fig. 3.1) by conversion of the complicated shape into polar coordinate space and the subsequent Fourier decomposition. The periodicity of the sines and cosines refers to the number of 'lobes' in the shape whereas their amplitude coefficients control the degree of lobe differentiation. As radial Fourier analysis utilizes the equiangular sequence-based sampling criterion [62], the

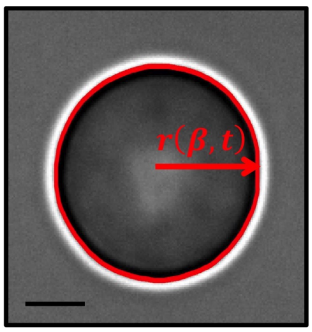

Figure 3.2: Spline-fitted polar coordinates of the membrane edge contour line remove artifacts due to pixelation and decouple its fluctuations from translational motion of the RBC's center of mass. Scale bar: 2 µm.

Cartesian coordinates of the RBC's contours for each frame of the movie (see chapter 2.4) are converted and spline-fitted to polar coordinates with the radius $r(\beta, t)$ at equiangular distances β of 0.5°(Fig. 3.2). Due to the spline fitting and inevitable mean-centering of the contour line during this conversion of coordinate systems, artifacts resulting from pixelation are removed and the translational motion of the RBC is further intrinsically decoupled from its remaining motion. The $n = 720$ polar coordinates are partitioned into a Fourier function,

$$r(\beta, t) = \bar{r}(t) + \sum_{q=1}^{m} \left(a_q(t) \cdot cos(q \cdot \beta) + b_q(t) \cdot sin(q \cdot \beta) \right) \tag{3.1}$$

where $m = n/2 - 1$ and the coefficients $a_q(t)$ as well as $b_q(t)$ control the amplitudes of the sine and cosine functions and therefore determine the detailed shape of the membrane edge contour line, whose size is given by the mean radius vector $\bar{r}(t)$ around the RBC's center of mass. In particular, $a_q(t)$ and $b_q(t)$ are calculated by means of multiple trigonometric regression analysis, i.e., fitting the empirical shape of the RBC to a set of harmonic figures one-by-one through adjustment of the amplitude coefficients by

$$a_q(t) = \frac{2}{n} \sum_{i=1}^{n} r_i(t) \cdot cos(q \cdot \beta_i) \tag{3.2}$$

$$b_q(t) = \frac{2}{n} \sum_{i=1}^{n} r_i(t) \cdot sin(q \cdot \beta_i) \tag{3.3}$$

where r_i and β_i are the polar coordinates of the RBC's spline-fitted contour line.

In order to decouple the overall morphology of the membrane edge not only from the translational but also from the rotational motion of the RBC, the Fourier function 3.1 is expressed by avoiding two separate amplitude-based shape descriptors [63],

$$r(\beta, t) = c_0(t) + \sum_{q=1}^{m} (c_q(t) \cdot cos(q \cdot \beta + \phi_q(t))) \tag{3.4}$$

where $c_q(t) = \sqrt{(a_q(t))^2 + (b_q(t))^2}$ and $\phi_q(t) = \arctan(a_q(t)/b_q(t))$. In particular, $c_q(t)$ are the amplitudes and $\phi_q(t)$ are the phases of the harmonic q, both representing a set of q independent and uncorrelated shape variables for each frame t. The zeroth harmonic amplitude $c_0(t)$ describes a circle with the mean radius of the RBC around its center of mass, the first one $c_1(t)$ the contribution of an offset circle, the second harmonic amplitude $c_2(t)$ the amount of elongation, the third $c_3(t)$ a trefoil and so on.

3.2 Rotational Motion of the RBC and Flickering Amplitude of its Membrane Edge

Information about the angle of best-fit rotation for these harmonic figures to a position of maximum correspondence with the observed boundary outline of the RBCs is contained in $\phi_q(t)$. Consequently, the phase of the first non-circular Fourier frequency, $\phi_{q=2}(t)$, can be used to estimate the amount of rotation exhibited by the RBCs (Fig. 3.3). The trajectory and its deviation from the mean value of $\phi_{q=2}(t)$,

$$\left\langle \phi_{q=2}^2 \right\rangle = \left\langle \left(\phi_{q=2}(t) - \langle \phi_{q=2} \rangle\right)^2 \right\rangle \tag{3.5}$$

for a single RBC inside a chamber (Fig. 3.4) indicates that the rotational motion in the image plane is also diffusive. Here, $\phi_{q=2}(t)$ is the phase of the second Fourier frequency as a function of time after starting the bright-field imaging and $\left\langle \phi_{q=2}^2 \right\rangle$ is the corresponding mean during a time interval of $t = 30\,\mathrm{s}$. Taking into account that for one-dimensional rotational diffusion, $\left\langle \phi_{q=2}^2 \right\rangle = 2D_r t$, the trajectories of $\phi_q(t)$ finally result in a rotational diffusion constant of $D_r = \left\langle \phi_{q=2}^2 \right\rangle / 2t = (1.1 \pm 0.8) \cdot 10^{-2}\,\mathrm{rad}^2/\mathrm{s}$ for the RBCs inside the microchambers.

Through partitioning the contour lines of the RBCs into the Fourier function 3.4, the analysis of the global membrane edge fluctuations can now be

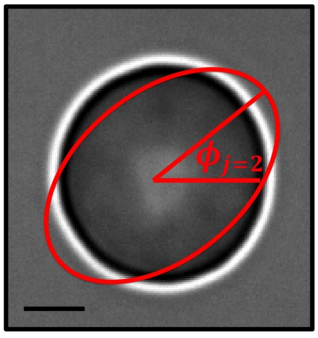

Figure 3.3: Phase angle of the (exaggerated) first non-circular Fourier harmonic yields information about the RBC's rotational motion. Scale bar: 2 µm.

based on a translationally and rotationally invariant description by using their harmonic amplitudes $c_q(t)$. The time-averaged amplitude spectrum for the first 20 harmonics of a typical single RBC inside a microchamber is shown in Fig. 3.5a and summation over all harmonics of the deviation from the time average,

$$\delta = \sum_{q=0}^{n} \left(c_q(t) - \langle c_q \rangle \right) \tag{3.6}$$

leads to the corresponding fluctuation histogram (Fig. 3.5b). Fluctuations of the membrane global edge $\sqrt{\langle U^2 \rangle}$ are determined from the Fourier harmonic amplitudes $c_q\,(t)$ by

$$\sqrt{\langle U^2 \rangle} = \sqrt{\sum_{q=0}^{n} \left\langle \left(c_q(t) - \langle c_q \rangle \right)^2 \right\rangle} \tag{3.7}$$

using a series of $9{\cdot}10^4$ consecutive images. The first fluctuation mode, $\left\langle U_{q=1}^2 \right\rangle$, can be further related to the bending modulus of the RBCs [19],

$$\kappa = \frac{6 \cdot 10^{-3}\, k_B T R^2}{\left\langle U_{q=1}^2 \right\rangle} \tag{3.8}$$

where R is the cell radius.

Due to their passive confinement inside microchambers and the precise control of their microenvironment, single non-adherent RBCs can not only be investigated in unprocessed blood conditions, but can further be analyzed under various conditions, e.g., diffusively washing the chambers via the controlling channel with different buffer solutions (Fig. 3.6). Under initial unprocessed blood conditions, we obtain $\sqrt{\langle U^2 \rangle}_{blood} = (21.9 \pm 1.8)\,\mathrm{nm}$ and $\kappa_{blood} = (7.1 \pm 1.3) \cdot 10^{-19}\,\mathrm{J}$. After diffusive washing of the chambers by flushing the controlling channel with isotonic phosphate-buffered saline (PBS, Fig. 3.6a) containing 1 mg/ml bovine serum albumin (BSA) and 10 mM glucose (Sigma-Aldrich, Saint Louis, USA) using appropriate tubing and syringe pumps (Cetoni GmbH, Germany), the RBCs retained their motion and the membrane edge fluctuations of the same population

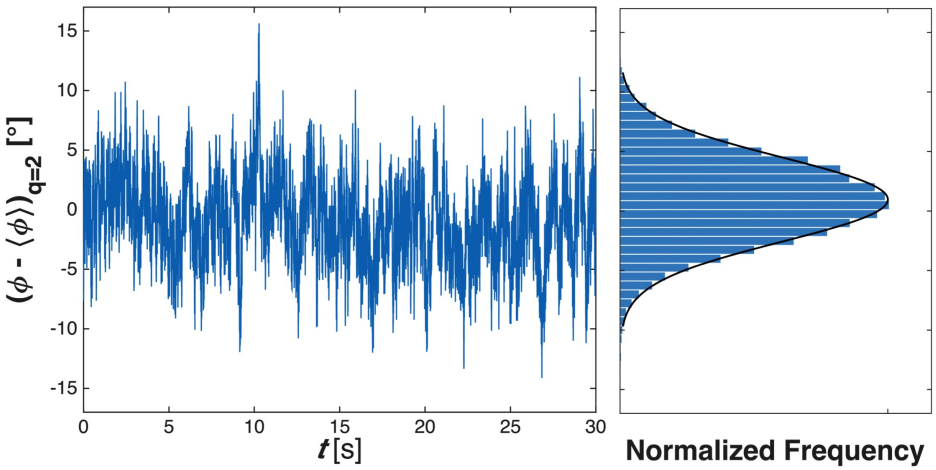

Figure 3.4: Typical time record and the deviation from the mean value of the phase angle of the second Fourier harmonic shows that the rotational motion of RBCs in the image plane is also random walk-like. Reprinted and modified from Ref. [1].

changed marginally. Under these conditions, $\sqrt{\langle U^2 \rangle}_{buffer} = (21.1 \pm 2.1)\,\mathrm{nm}$ and $\kappa_{buffer} = (7.4 \pm 1.6) \cdot 10^{-19}\,\mathrm{J}$, which is in good agreement with values of $\sqrt{\langle U^2 \rangle}_{buffer}$ and κ_{buffer} from steady state measurements in the literature [19–21].

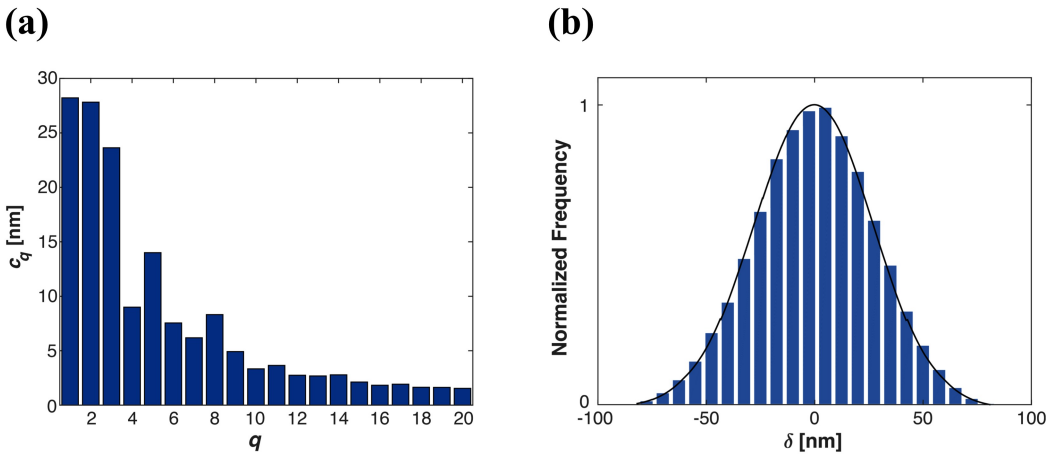

Figure 3.5: (a) Typical time-averaged amplitude spectrum for the first 20 harmonics of a RBC inside a microchamber and (b) summation over all harmonics of the deviation δ from their corresponding time average. Reprinted and modified from Ref. [1].

The viscoelastic membrane of the anucleate RBC forms its only structural component and it accounts for all of the RBC's diverse as well as unique characteristics [14]. It is a composite structure, consisting of a cytoskeleton network that is linked to a lipid bilayer via intramembrane proteins and represents the most thoroughly studied prototype of a compound membrane [11]. Mechanically stable morphologies of the RBC are assumed to represent energy minima of the plasma membrane under the constraint of fixed surface area and cell volume [27]. The spontaneous curvature C_0 of the membrane [64] and a preferred area difference ΔA_0 between the inner and outer leaflet of the membrane bilayer [65] are incorporated in the so-called area-difference-elasticity (ADE) model [66],

$$E_{ADE} = \frac{\kappa}{2} \oint_S (H - C_0)^2 dS + \frac{\bar{\kappa}\pi}{A_{RBC} d_m^2} (\Delta A - \Delta A_0)^2 \tag{3.9}$$

where κ and $\bar{\kappa}$ are the local and non-local bending elastic moduli, H is the local mean curvature of the membrane, A_{RBC} is the total area of the cell, d_m is the membrane thickness and ΔA is the area difference between the two leaflets. The ADE Model is based on the assumption that all chemical,

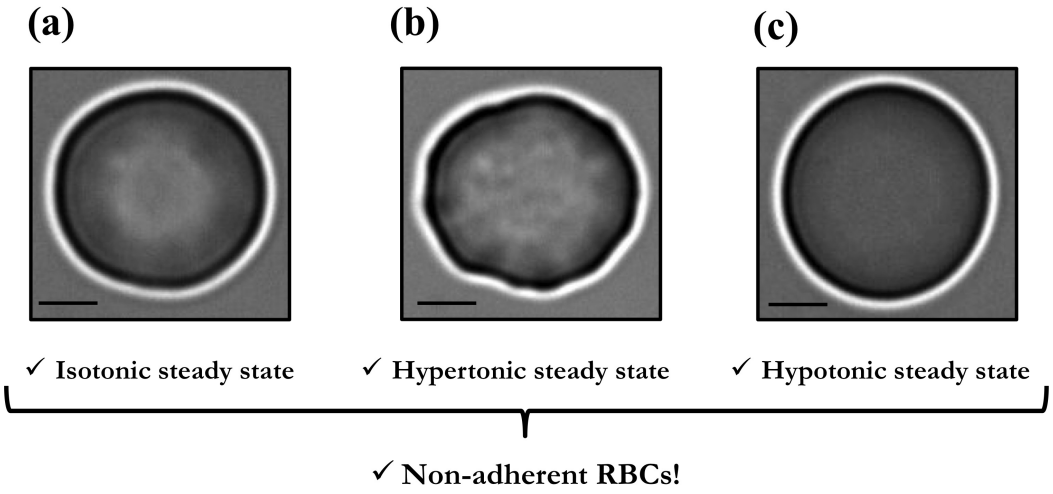

Figure 3.6: Typical non-adherent RBCs in osmotic steady states after diffusive washing of the microchambers by flushing the controlling channel with (a) isotonic, (b) slightly hypertonic and (c) hypotonic buffer solution. Scale bars: 2 µm.

biological or even physical shape-changing agents act through their effect on ΔA_0 and biochemistry only influences to what extend and how each agent modifies the preferred area difference [27]. Taking into account that $d_m \approx 4$ nm and therefore much smaller than the typical RBC radius $R \approx 4\,\mu$m, the area difference can be approximated to $\Delta A \approx d_m \oint_S H dS$ [28]. Consequently, the bilayer energy of the membrane as defined by the ADE model is proportional to the integrals of the local mean curvature H and its square H^2 over the cells' closed surface, i.e., $E_{ADE} \sim \oint_S H dS$ and $E_{ADE} \sim \oint_S H^2 dS$. Adding the elastic energy E_{cyt} of the spectrin-based cytoskeleton [67] to E_{ADE} results in full RBC elastic energy, $E_{RBC} = E_{ADE} + E_{cyt}$.

The local two-dimensional curvature $1/R$ of the RBC's membrane edge in isotonic conditions are almost exclusively concave with $1/R > 0$ (Fig. 3.7a, dark blue) and show only minor sections of convexity, i.e., $1/R < 0$ (Fig. 3.7a, turquoise). Slightly increasing the osmolarity of the RBC's microenvironment by diffusive washing with hypertonic buffer (550 mOsm) containing additional 7.9 mg/ml NaCl results in a slight decrease in cell volume and a small increase in cell membrane edge fluctuations with $\sqrt{\langle U^2 \rangle}_{hyper} = (26.7 \pm 2.3)$ nm and the corresponding decrease in bending stiffness $\kappa_{hyper} = (5.4 \pm 1.5) \cdot 10^{-19}$ J

(Fig. 3.6b). This rise in membrane fluctuation amplitude for slightly hypertonic environments has been suggested to result from the small decrease in membrane tension accompanying the modest reduction in cell volume [20]. Additionally, the RBC's local curvatures are not only indicating the increase in local concavity (Fig. 3.7b, dark blue), but are also showing the formation of locally convex segments along the membrane contour (Fig. 3.7b, turquoise). Both effects lead to an increase of E_{ADE} and the mechanism of this process is proposed to involve small changes in the relaxed area difference between the two leaflets of the RBC's plasma membrane [65]. In particular, any effect that expands the outer leaflet relative to the inner one produces a tendency to form convex structures on the cell surface to accommodate the extra area [27] and the growth of protrusions consequently represents a natural way to favor the expansion of the outer leaflet [29].

Exposing the RBCs to hypotonic conditions (200 mOsm) by flushing the controlling channel with diluted buffer (2/3 isotonic buffer, 1/3 water) leads to a swelling of the cells with a reduced membrane edge fluctuation amplitude of $\sqrt{\langle U^2 \rangle}_{hypo} = (10.3 \pm 1.6)\,\mathrm{nm}$ and a large increase of bending stiffness to $\kappa_{hypo} = (2.0 \pm 0.2) \cdot 10^{-18}\,\mathrm{J}$ (Fig. 3.6c).

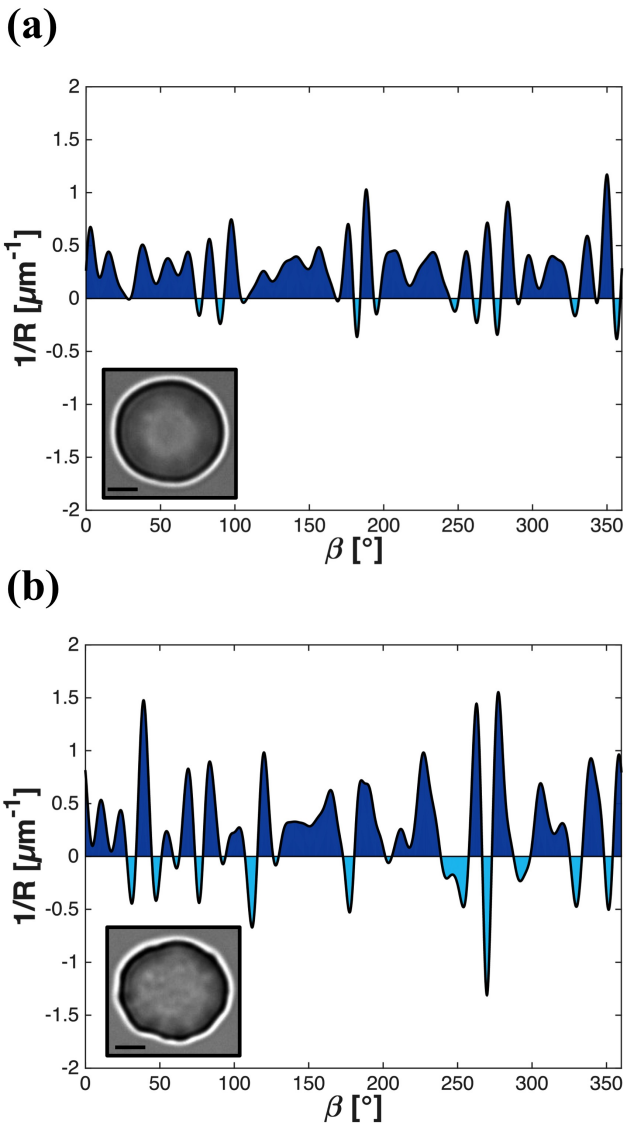

Figure 3.7: Local two-dimensional curvatures of a typical RBC under different buffer conditions. (a) In an isotonic environment $1/R$ shows presence of dominantly concave membrane structures ($1/R > 0$, dark blue) with an insignificant fraction of convex parts ($1/R < 0$, turquoise) along the cell's contour, whereas under (b) slightly hypertonic buffer conditions $1/R$ indicates the increase of concavity ($1/R > 0$, dark blue) as well as the significant formation of convex membrane structures ($1/R < 0$, turquoise). Scale bars: 2 µm.

3.3 Flickering Analysis - Towards the Dynamics of Single RBCs in Unsteady States

Due to diffusion-controlled material transport into the flow-free microchambers and *vice versa*, analysis of single RBCs inside our device is not limited to constant microenvironments and therefore allows for investigations of their dynamics in unsteady states. In particular, our microfluidic design enables the time-resolved measurement of membrane edge flickering of non-adherent RBC's during the morphological response to a variation of osmolarity after changing the buffer in the controlling channel (Fig. 3.8a).

In analogy to the steady state measurements, the device is first washed with isotonic buffer via the controlling channel after its' self-filling with unpro-

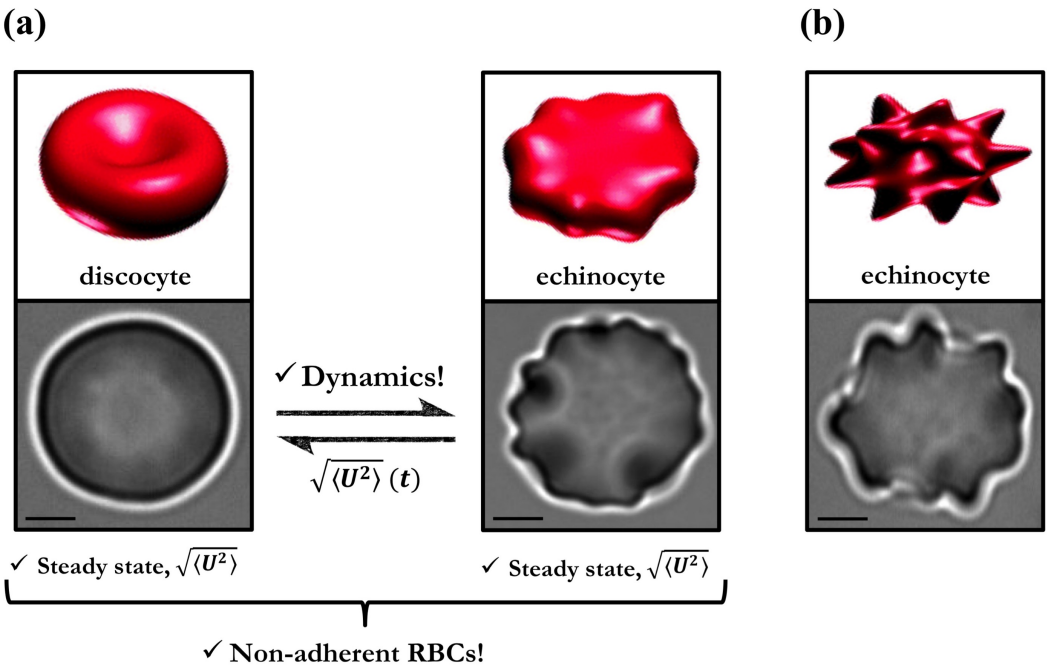

Figure 3.8: Precise control of the RBC's microenvironment enables the dynamic measurement of RBC flickering during the reversible shape evolution from the discocyte to the echinocyte morphology. The osmolarity is adjusted to result in a quasi-two-dimensional membrane edge deformation (a) since a further increase in hypertonicity leads to protrusions out of the image plane (b). Scale bars: 2 µm. Simulation images (top) reprinted and modified from Ref. [68].

cessed blood and a discocyte-shaped RBC inside one of the microchambers is selected for fast bright-field imaging. The osmolarity Π is increased by diffusive washing of the microchamber through flushing the controlling channel with hypertonic buffer ($\Pi = 1088\,\mathrm{mOsm}$), containing polystyrene beads ($1\,\mu\mathrm{m}$ diameter, Polysciences) in order to precisely trace its arrival at the connecting channel. In particular, the osmolarity of the hypertonic buffer solution is chosen to result in a deformation of the RBC's membrane edge that still allows the detection of the contour line by means of standard image processing algorithms (Fig. 3.8a), i.e., two-dimensional deformation in the image plane. Further increase of the osmotic concentration would result in significant membrane edge deformation out of the image plane (Fig. 3.8b) and consequently would not permit RBC flickering analysis by means of the presented radial Fourier method.

After the disco-echinocyte transition of the RBC is completed, the device is washed with an identical hypertonic solution lacking PS beads. Finally, the microchamber is again washed diffusively by flushing the controlling channel with isotonic buffer including PS beads to initiate and trace the transition of the RBC back to the discocyte morphology. Before and after each diffusive washing period, the steady states of the RBC were recorded and resulted in the corresponding membrane edge fluctuation amplitudes $\sqrt{\langle U^2 \rangle}$ (Fig. 3.9, blue points). Material transport into the microchambers and *vice versa* is precisely controlled by diffusion and the time that elapsed since the traced onset of the buffers at the connecting channel is therefore directly related to the osmolarity at the position of the RBC inside the chamber (see Eq. 2.2). As a result, $\sqrt{\langle U^2 \rangle}$ can be further analyzed dynamically on the single cell level during the whole disco-echino-discocyte transition (Fig. 3.9, blue lines) by taking into account running intervals of $9 \cdot 10^4$ consecutive images instead of a singular set as used in the steady state measurements.

The membrane edge fluctuation analysis during the reversible shape evolution of individual RBCs inside microchambers is shown in Fig. 3.10. In the initial isotonic steady state, the membrane fluctuation amplitude of discocyte-shaped RBCs is $\sqrt{\langle U^2 \rangle}_{iso,initial} = (20.8 \pm 2.3)\,\mathrm{nm}$ and the arrival of the hypertonic buffer at the connecting channel to the microchamber in-

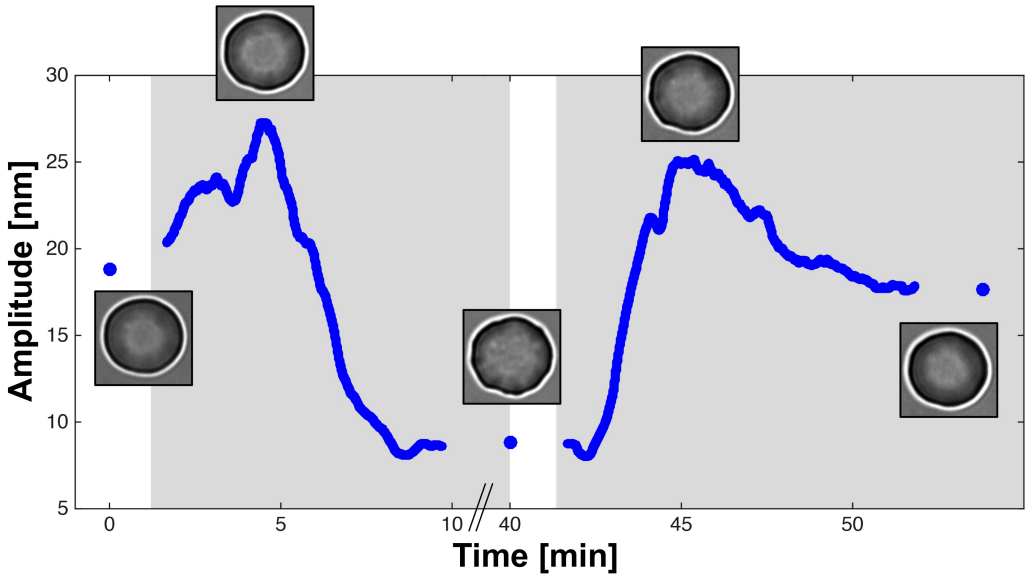

Figure 3.9: Typical morphologies during the reversible disco-echinocyte transition with the corresponding membrane edge fluctuations of a non-adherent RBC as function of time after the arrival of the exchange buffers. Bright-field images of intermediate morphologies during the transition are shown at maximum amplitudes as well as at isotonic and hypertonic steady states. Reprinted and modified from Ref. [1].

duces the disco-echinocyte transitions. During this shape transformation, the membrane edge fluctuations first increase substantially to a maximum of $\sqrt{\langle U^2 \rangle}_{max,iso\rightarrow hyper} = (27.9 \pm 2.8)\,\mathrm{nm}$ at intermediate morphologies, before largely decreasing to $\sqrt{\langle U^2 \rangle}_{hyper} = (8.7 \pm 1.5)\,\mathrm{nm}$ for the final echinocytes in the hypertonic steady state. The rise in membrane fluctuation amplitude for intermediate morphologies during the disco-echinocyte transformation results from the modest reduction in cell volume during the early stages of the transition and is in agreement with $\sqrt{\langle U^2 \rangle}_{hyper}$ obtained from the steady state measurements at slightly hypertonic conditions. However, the steep rise in hemoglobin concentration eventually leads to the suppression of the membrane fluctuations in the final echinocyte shape at $\Pi = 1088\,\mathrm{mOsm}$.

Diffusive washing of the microchamber with isotonic buffer starts the transition back to the discocyte. Fluctuations of the membrane edge again in-

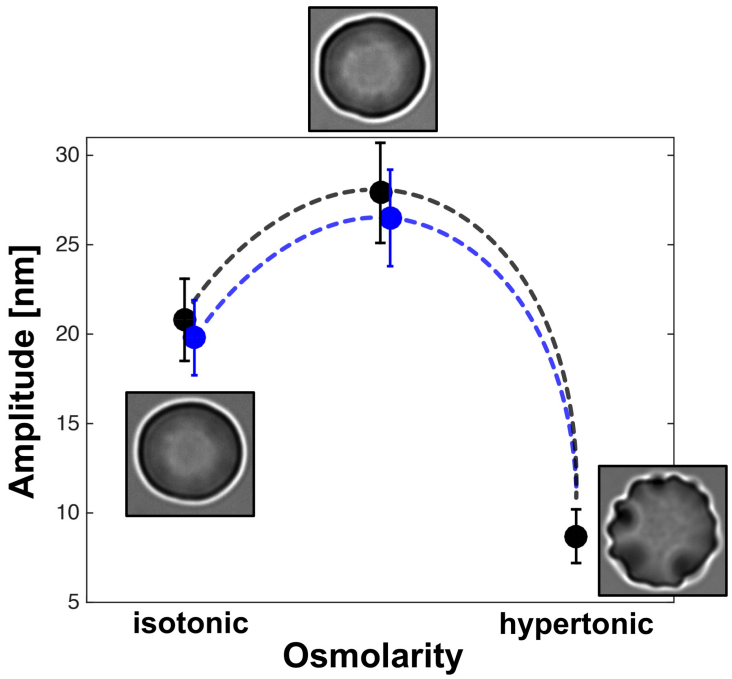

Figure 3.10: Membrane edge fluctuation analysis of functional RBCs during reversible disco-echinocyte transformations under altering osmolarity. Black symbols and lines (guides to the eye) indicate the evolution of the membrane fluctuations from the initial isotonic steady states via the intermediate shapes with maximum amplitudes to the final hypertonic steady states, whereas blue symbols and lines (guides to the eye) indicate the reversible process back to the restored biconcave shapes under isotonic conditions. Reprinted and modified from Ref. [1].

crease to a maximum of $\sqrt{\langle U^2 \rangle}_{max,hyper \rightarrow iso} = (26.5 \pm 2.7)\,\mathrm{nm}$, before reaching the restored isotonic steady state with $\sqrt{\langle U^2 \rangle}_{iso,restored} = (19.8 \pm 2.1)\,\mathrm{nm}$. The bright-field optical images of the restored isotonic discocyte morphologies and the marginal difference of $\sqrt{\langle U^2 \rangle}_{iso,restored}$ compared to the initial isotonic state indicate that the disco-echino-discocyte transition is largely reversible.

One of the fundamental questions regarding RBCs that still remains controversial is whether the fluctuations of the membrane are driven by an active process or are simply thermal motion [22]. Using our specialized device, the time-resolved analysis of a single RBC's morphological response with its related alterations of the membrane edge fluctuation amplitude shows a timescale of about 10 minutes. This is significantly slower than the change in

osmolarity at the RBC's position inside the microchamber via diffusive washing. In particular, the grey areas in Fig. 3.9 correspond to the time when already more than 90% of excess NaCl diffused from the controlling channel to the position of the RBC inside the microchamber ($\Pi > 1009\,\mathrm{mOsm}, \textit{isotonic} \rightarrow \textit{hypertonic}$) and *vice versa* ($\Pi < 379\,\mathrm{mOsm}, \textit{hypertonic} \rightarrow \textit{isotonic}$), i.e., when the osmolarity inside the chamber already reached a steady state. Water transport across the membrane of human RBCs is extremely fast, changing the cell's water content in a time-scale of about 20 ms at room temperature [69]. Therefore, RBC membrane permeability to water as a limiting factor is unlikely to explain the observed time delay of the morphological response and its corresponding alterations in fluctuation amplitude to changes in osmolarity, which might support studies suggesting active membrane processes contributing to RBC flickering [21, 22, 70].

By overcoming the limitations of available approaches to single RBC experiments, the dynamic measurement of non-adherent RBCs' morphological responses to increasing osmolarity became feasible. However, the application of our method is not limited to the investigation of RBC flickering or shape transformations, but can be further regarded as a general system in order to investigate the temporal behavior of single RBCs under precise control of their environment. Studies of single RBCs exposed to external stimuli will provide important insights into their fundamental biophysical properties, which is an essential step towards a better understanding of the most abundant cell type in the human body.

Chapter 4

Spectroscopic Analysis of Single Functional RBCs[†]

The horizontal confinement of single RBCs in flow-free microchambers offers an optimal environment not only to investigate mechanical properties of the membrane, but also to further apply advanced optical methods in order to study molecular processes within the cell. In particular, RBC abnormalities are not limited to impaired mechanical properties of the membrane, where flickering analysis shows promising potential for disease diagnosis, but are also affecting the oxygenation capability which is determined by the hemoglobin (Hb) composition in the cytoplasm. A process within RBCs that is well-known to be sensitive to photo-dissociation is the binding of oxygen to Hb [71]. Here, Raman spectroscopy is suited especially to investigate RBCs due to water generally not interfering with Raman spectral analysis. In particular, Raman microscopy has emerged as a powerful technique to investigate molecular processes within single RBCs [32, 72–75]. So-called Raman tweezers, which is the coupling of Raman spectroscopy with optical tweezers, have been successfully used to distinguish between healthy and diseased cells in thalassemia [75, 76]. Thalassemias are inherited blood disorders in which the body produces an abnormal form of hemoglobin, i.e., a genetic defect causes a reduced rate of synthesis of one of the globin chains which can result in various signs and symptoms [74].

[†]This chapter is partially reprinted and modified from Ref. [1].

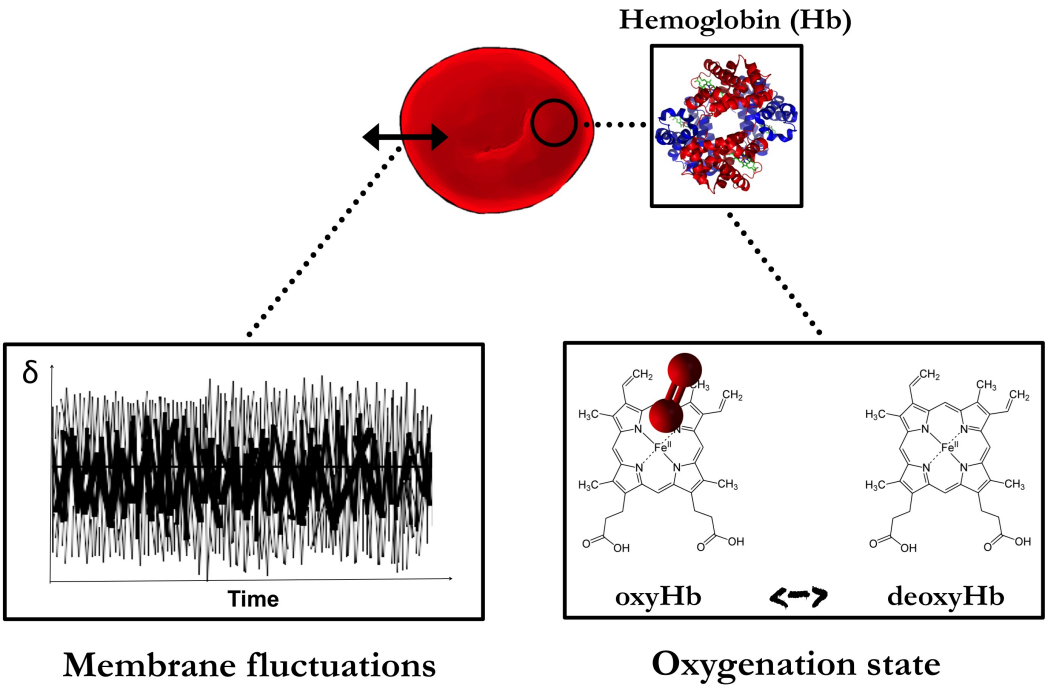

Figure 4.1: Horizontal confinement of the RBCs inside the microchambers offers an optimal environment to study both, the mechanical properties of the RBC via its membrane fluctuations (left) as well as molecular processes inside the cytoplasm, e.g., the photo-induced dissociation of oxygen from Hb (right).

4.1 Raman Spectroscopy - Inelastic Scattering of Light

Raman spectroscopy is a powerful spectroscopic method which is commonly used to provide a molecular fingerprint of the system under study [77]. In particular, Raman spectroscopy relies on the inelastic scattering of monochromatic light (Fig. 4.2), usually from a laser in the visible, near infrared, or near ultraviolet range of the electromagnetic spectrum. The scattering results from the interaction of the light with molecular vibrations and a change in molecular polarisability is further required during the vibration for the Raman effect to occur. However, most of the scattered light is elastic scattered radiation at the wavelength corresponding to the laser line (Rayleigh scatter-

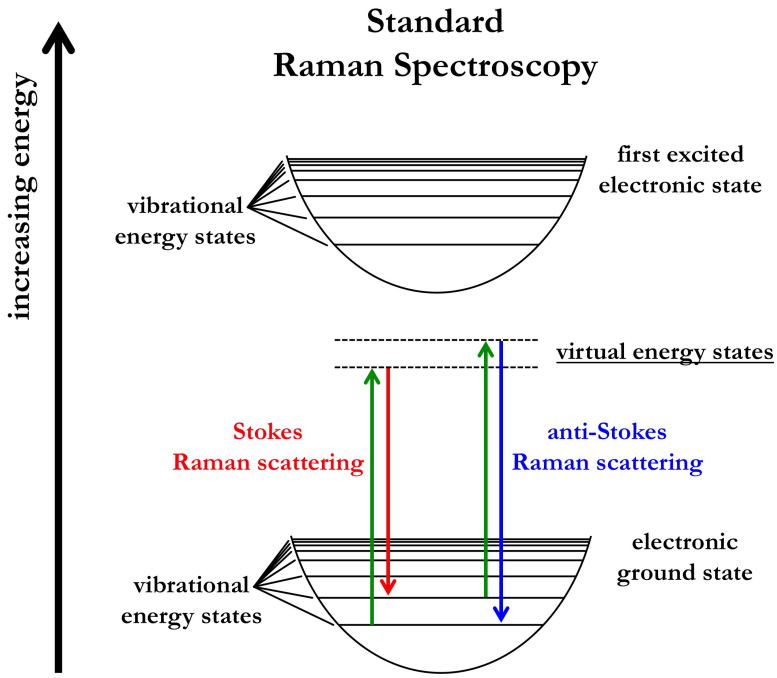

Figure 4.2: Schematic illustration of inelastic scattering in standard Raman spectroscopy. The laser excitation (green upwards arrows) is much higher in energy than the molecular vibrations and the frequency of the photon is either lower (Stokes Raman scattering, red downward arrows) or higher (anti-Stokes Raman scattering, blue downward arrows) in Raman scattering.

ing), while only a minute fraction of the photons lost or gained energy during this process. This shift in energy, the so-called Raman shift, occurs due to partial exchange of the photon's energy with molecular vibrations of the system and therefore yields information about its specific vibrational modes. Although the photons can either loose energy due to the inelastic scattering (Stokes Raman scattering) or gain energy during this process (anti-Stokes Raman scattering), the latter is rarely used as it gives an even weaker signal in the Raman spectrum. Nevertheless, both processes generally lead to very weak signals in traditional Raman spectroscopy as it uses laser excitation at any wavelength in order to measure the Raman scattering of the applied laser light.

In contrast, resonance Raman spectroscopy (Fig. 4.3) carefully chooses

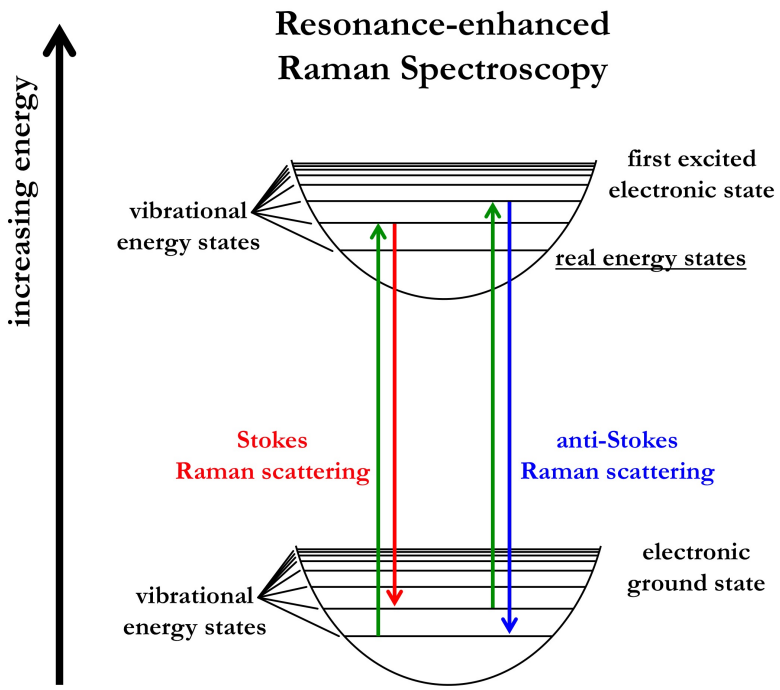

Figure 4.3: Schematic illustration of inelastic scattering in resonance-enhanced Raman spectroscopy. The laser excitation (green upwards arrows) is again much higher in energy than the molecular vibrations, but is further chosen to overlap with an electronic transition of the molecule and therefore provides enough energy to excite the electrons to a higher electronic state.

the excitation wavelength to overlap with an electronic transition of the investigated molecule, leading to a strong enhancement of the Raman intensity by a factor of $10^2 - 10^6$ [78,79] and therefore significantly decreases the detection limit. This is particularly useful for the investigation of single RBCs as resonance Raman scattering from Hb occurs only at its prosthetic group due to molecular absorption in the visible and near ultraviolet region being restricted to this specific part of the molecule [80]. In particular, the porphyrin groups in hemoglobin (Hb) lead to absorption of visible light and if the Raman excitation wavelength matches a transition wavelength of these functional groups, a selective resonance enhancement of the porphyrin Raman signal occurs, without spectral interference from the sourrounding globin or other parts of the RBC [30,80–82]. The Raman bands at $1640\,\mathrm{cm}^{-1}$, $1582\,\mathrm{cm}^{-1}$ and $1378\,\mathrm{cm}^{-1}$ are characteristic for the oxygenated form of human hemoglobin (oxyHb) and undergo a shift to $1604\,\mathrm{cm}^{-1}$, $1553\,\mathrm{cm}^{-1}$ and $1355\,\mathrm{cm}^{-1}$ upon transition to the deoxygenated form (deoxyHb). Applying high laser intensities leads to a photo-induced conversion of oxyHb (Fe^{2+}) to the inactive metHb (Fe^{3+}) state, where the oxygen is irreversibly bound to the heme group [32].

4.2 Setting the Stage - About a Custom-Built Confocal Raman Microscope

We used a custom-built confocal Raman microscopy setup for parallel bright-field and spectral imaging to investigate the photo-induced oxygenation cycle of single, non-adherent RBCs confined inside the microchambers (simplified scheme: Fig. 4.4, Photograph: Fig. 4.5). A 532 nm continuous wave, diode-pumped solid-state laser (SOLE laser system, Omicron, Rodgau-Dudenhofen, Germany) is coupled into a single-mode optical fiber (Omicron, Rodgau-Dudenhofen, Germany) and used for resonance Raman excitation. The laser beam gets aligned by two high reflectance mirrors (MaxMirror, Semrock, Rochester, USA) to the optical axis of an optomechanical rail system (LINOS Microbench, Qioptiq Photonics, Göttingen, Germany), mounted

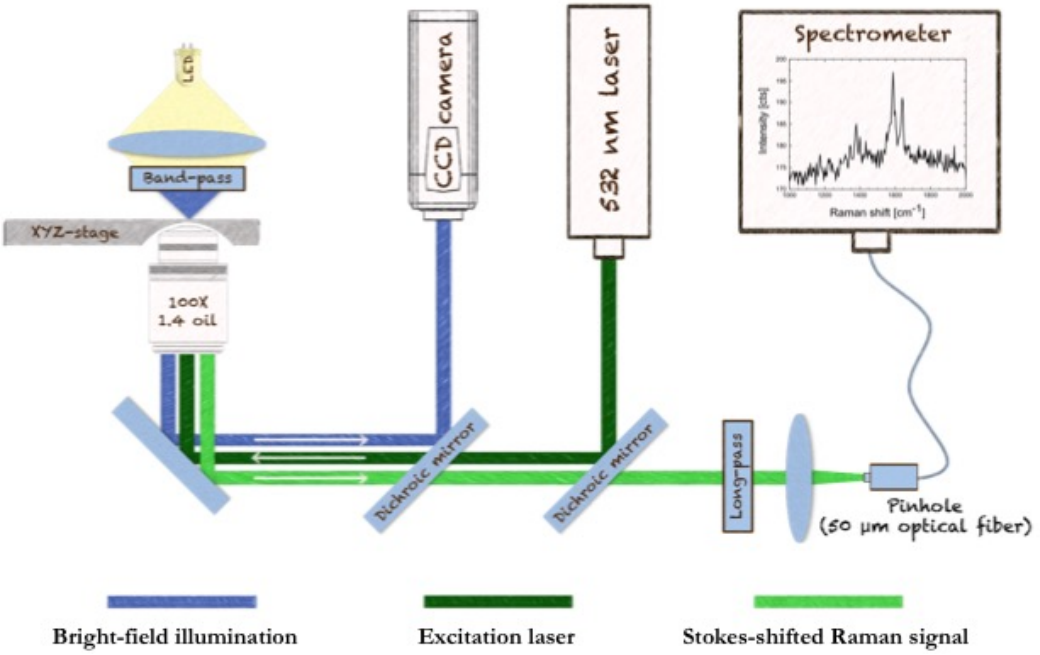

Figure 4.4: Simplified scheme of the custom-built confocal Raman setup for parallel microscopic and spectroscopic investigations of single RBCs confined inside the microchambers.

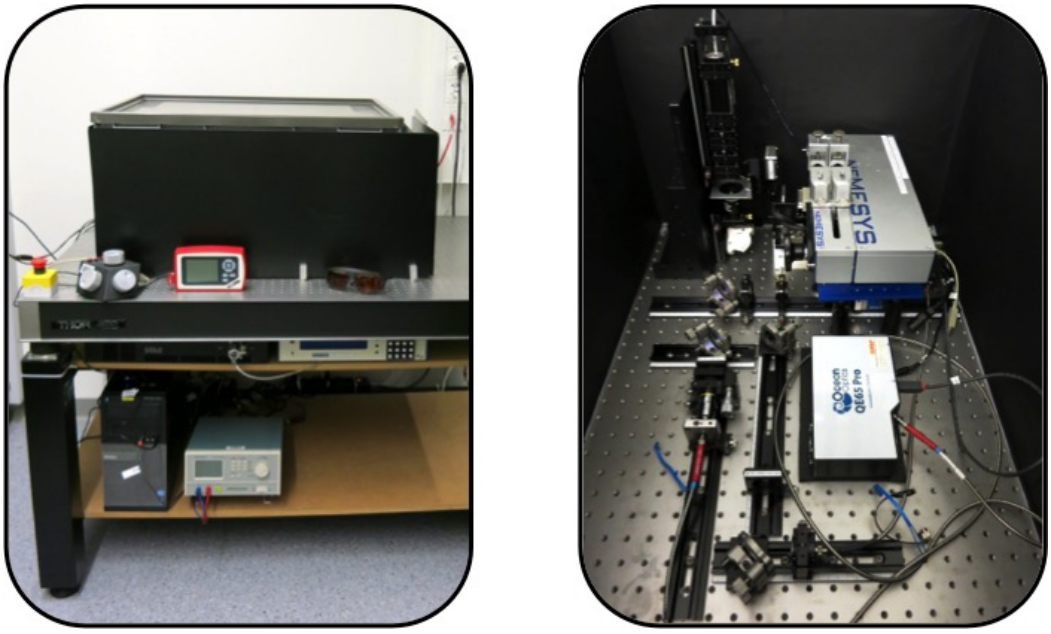

Figure 4.5: Photograph of the custom-built, table-top confocal Raman setup.

on a passively vibration isolated optical table (Thorlabs, Newton, USA). The aligned laser beam first passes a 532 nm long-pass and a 458 nm short-pass dichroic mirror (RazorEdge, Semrock, Rochester, USA) before being reflected by another high reflectance mirror and focused on the sample with a 100x (N.A. 1.4) PlanApo oil immersion objective (Olympus, Tokyo, Japan). The signal originating from Stokes Raman scattering passes both dichroic beam-splitters, a 532 nm edge filter for removing the remaining elastically scattered Rayleigh signal and finally gets collected into a 50 µm multimode optical fiber (Ocean Optics, Dunedin, USA) acting as a pinhole and connected to a spectrometer (QE65 Pro-Raman, Ocean Optics, Dunedin, USA). Simultaneously, the blue part of the electromagnetic spectrum from a white light-emitting diode (Cree, Durham, USA) passes through a 445 nm short-pass filter (RazorEdge, Semrock, Rochester, USA) and illuminates the sample through a combination of lenses and diaphragms (Qioptiq Photonics, Göttingen, Germany) in order to implement the Köhler illumination technique. The resulting bright-field image of the sample is reflected by the 458 nm short-pass dichroic

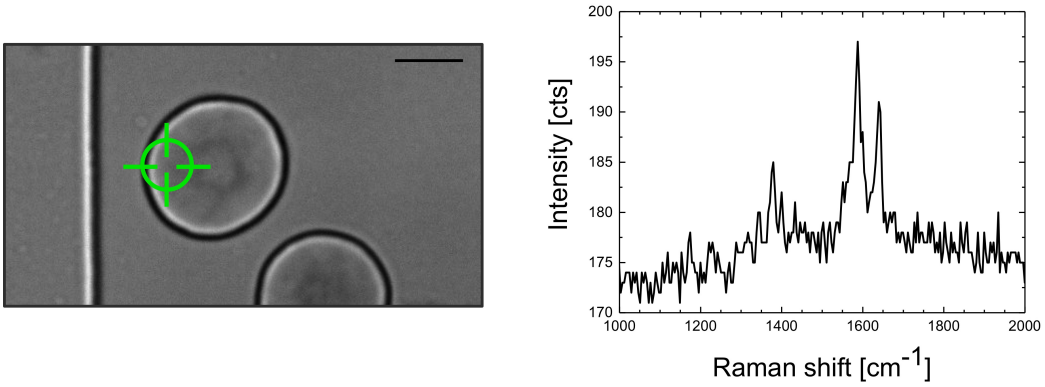

Figure 4.6: As the position of the excitation laser is known after calibration, our custom-built confocal Raman setup combines spatial (left) with spectral information (right) and therefore enables parallel bright-field and chemical imaging of single functional RBCs. Scale bar: 4 µm.

mirror towards a charge-coupled device (CCD) camera (pco.pixelfly, PCO, Kelheim, Germany) and therefore enables parallel bright-field and chemical imaging of individual RBCs inside the microchambers (Fig. 4.6).

4.3 Overcoming Photo-Degradation - The Reversible Oxygenation Cycle of Functional RBCs

Although Raman microscopy has emerged as a powerful technique to investigate molecular processes within single RBCs [32, 72–75], the involved manipulations can cause difficulties with preserving the cell's integrity. Many of the available approaches to spectral analysis of single RBCs are based on so-called Raman tweezers [74–76, 83], which is the coupling of Raman spectroscopy with an optical tweezer and require rather high laser intensities in the order of several milliwatts to actively immobilize the cells.

Without the necessity of high-intensity optical tweezers for cell immobilization due to a passive confinement inside the microchambers, our approach drastically reduces the accumulated photon dose on the RBC. Consequently, analysis of the RBC's oxygenation state is not limited by photo-degradation and resonance Raman spectra of single functional RBCs with Hb solely in the oxygenated state are recorded. In particular, the power of the Raman excitation laser ($\lambda = 532\,\mathrm{nm}$) is chosen to be merely $1\,\mu\mathrm{W}$ before entering the microscope objective (Fig. 4.7a, bottom). Increasing the laser power to $180\,\mu\mathrm{W}$ already leads to a mixture between the oxygenated and deoxygenated Hb states within the cells (Fig. 4.7a, middle), whereas applying $400\,\mu\mathrm{W}$ results in complete photo-induced conversion to deoxyHb (Fig. 4.7a, top). Due to constant diffusive washing of the microchambers with fresh isotonic buffer via the controlling channel, the photo-dissociation is reversible when the excitation power is again decreased to $1\,\mu\mathrm{W}$. In order to further investigate the photo-induced deoxygenation process, we determined the background-corrected and normalized intensity ratio $I_{1582\,\mathrm{cm}^{-1}}/I_{1553\,\mathrm{cm}^{-1}}$ for various excitation powers (Fig. 4.8). Here, already a slight increase in laser intensity leads to a significant conversion of oxyHb to deoxyHb inside the RBCs with a critical excitation power of $P_{crit} = (88.3 \pm 3.7)\ \mu\mathrm{W}$.

In summary, the noninvasive, horizontal confinement in combination with a precise control over the cell's microenvironment represents ideal conditions

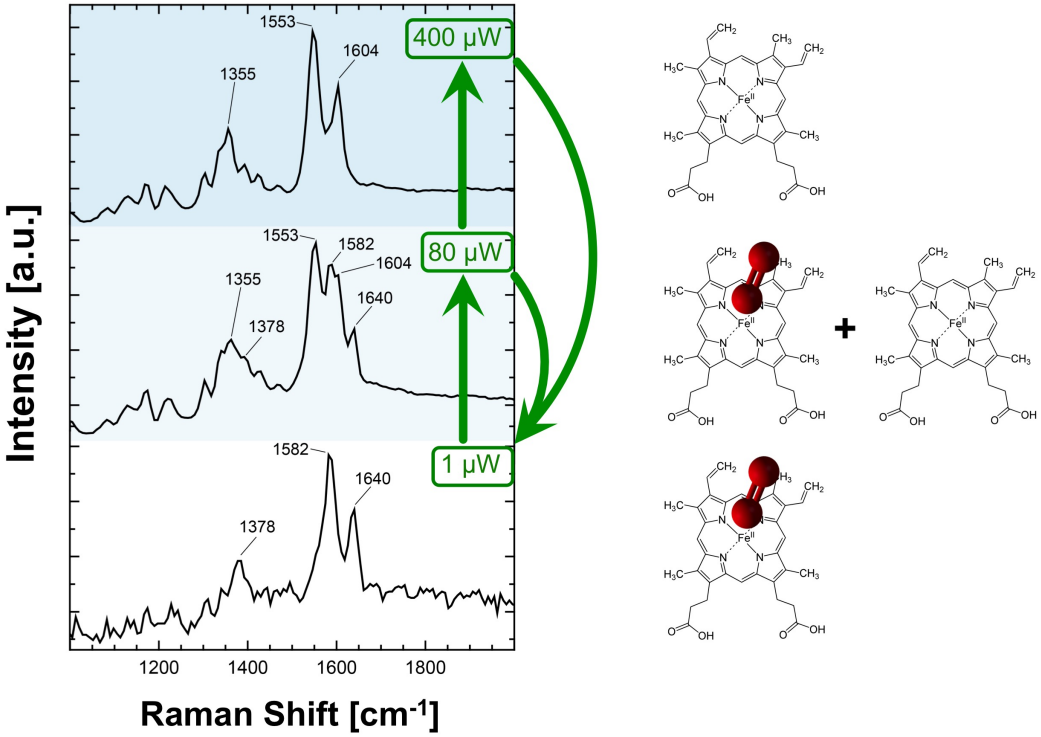

Figure 4.7: Resonance Raman spectroscopy of the reversible, photo-induced oxygenation cycle of single functional RBCs confined in microchambers: Typical resonance Raman spectra of a RBC inside a microchamber showing the change of the characteristic bands during the reversible photo-dissociation of oxygen from Hb. Integration time for each spectrum: 10 s. Reprinted and modified from Ref. [1].

for various microscopic or spectroscopic investigations on single functional RBCs. The confinement is also passive in the sense that no active immobilization by optical tweezers is needed, eliminating corresponding photodegradation or spurious photo-induced effects that inherently prohibit the access to reversible or long-term experiments on single functional RBCs. The accumulated radiation dose introduced through high-intensity trapping lasers can lead to hemolysis of RBCs [22] or induces the conversion of oxyHb to the inactive metHb state [32], both limiting the information that can be acquired by either microscopic or spectroscopic techniques. Our approach overcomes this limitation and combined with confocal resonance Raman spectroscopy we are able to record Raman spectra of functional individual RBCs purely

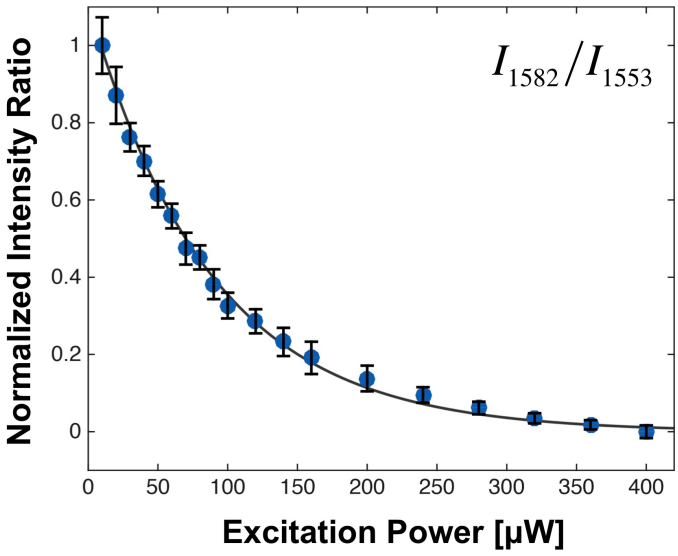

Figure 4.8: Background-corrected and normalized intensity ratio between the most prominent oxyHb ($1582\,\mathrm{cm}^{-1}$) and deoxyHb ($1553\,\mathrm{cm}^{-1}$) Raman bands as a function of increasing laser power during the photo-induced dissociation process of oxygen from Hb inside confined RBCs. Reprinted and modified from Ref. [1].

in the oxyHb state. We show that the laser power which is sufficient to already induce a conversion of oxyHb to deoxyHb inside the cell is in the µW range. This is only a fraction of what is typically applied in optical tweezers based methods [32, 74–76, 80, 83] and therefore may lead to difficulties of these approaches regarding their application to oxygenation-related RBC disorders. Although the application of very low laser powers to investigate hemoglobin-related phenomena strongly relies on the resonance enhancement of the very weak Raman signal when using a 532 nm laser, our unique approach can can serve as a general system to spectroscopically study single cells in a controlled microenvironment. Through adjusting the geometry of the microchambers and especially the connections between the chambers and the controlling channel, different cell types could be investigated by using an appropriate wavelength for Raman excitation.

Chapter 5

Single Macromolecule Dynamics - Actin Filaments in Microstructured Flow[†]

5.1 Actin as a Model System for Semiflexible Biopolymers

Actin is one of the most abundant proteins and found in essentially all eukaryotic cells [84]. The strength and flexibility of the RBC plasma membrane depends on a dense cytoskeletal network that underlies the entire membrane, is attached to it at many points and is mainly comprised of spectrin, filamentous actin (F-actin) and accessory proteins [14, 85]. Here, actin is in the form of short and extraordinarily stable filaments composed of 12 - 20 subunits, which is unique to the RBC since in other cells actin is present as more extensively polymerized filaments containing hundreds of monomers [86]. The cytoskeletal functionality is depending on a complex network and its relation to other properties and components of the cell is one of the prominent questions in biophysics [43]. The physics of many cells as well as of their surrounding are further to a great extent influenced by the properties of fibrous biopolymers. Analyzing their non-equilibrium behavior on the single macro-

[†]This chapter is partially reprinted and modified from Ref. [2].

molecule level represents an important step towards a better understanding of cellular dynamics and requires the exposure to of single filaments to hydrodynamic forces. Actin additionally serves as a general model system for semiflexible polymers [87, 88] and the behavior of individual macromolecular and biological filaments in confining geometries and microflows have apart from its fundamental relevance in biology a huge impact on materials science, biotechnology and chemical engineering [41, 89]. Especially, studies of the non-equilibrium dynamics and fluctuations of semiflexible polymers, having an elastic rigidity between the extremes of floppy, flexible polymers and rigid rods have recently attracted much attention [90, 91]. Suspending semiflexible filaments in viscous fluids may lead to buckling transitions in the presence of thermal fluctuations if the hydrodynamic forces dominate over the restoring elastic forces [90–93]. These conformational instabilities far from equilibrium [94], which show significant differences and new properties in comparison to equilibrium ones, can be studied experimentally [91, 95, 96] and in theoretical as well as simulation models [90–92, 97] by analyzing the transport of semiflexible polymers in microchannel flow. A detailed understanding of these dynamic processes of semiflexible filaments is of central importance for the analysis and sorting of biologically relevant polymers, e.g., DNA [98], as well as for the description of non-Newtonian flow behavior [99, 100] unusual transport in cellular flows [101] and pattern formation processes cytoplasmic streaming [102] where movement of molecular motors along cytoskeletal filaments in proximity to cell membranes may provide the motive force [103, 104].

5.2 Microfluidic Design - Exposing Single Actin Filaments to Hydrodynamic Forces

Non-equilibrium dynamics can be described as the behavior of a system when it is held far from thermal equilibrium by an external driving force [105]. In order to experimentally realize this situation for semiflexible biopolymers, single actin filaments are exposed to hydrodynamic forces by flows through spatially structured microchannels with alternating high- and low-velocity segments (Fig. 5.1). In particular, the microfluidic devices are designed for different channel width ratios of $A_n : A_w = 1 : 2$ ($A_n = 2\,\mu m$; $A_w = 4\,\mu m$) and $A_n : A_w = 1 : 4$ ($A_n = 2\,\mu m$; $A_w = 8\,\mu m$) with a length $B_n = B_w = 25\,\mu m$ of the narrow and wider channel regions at a constant height of $h = 2\,\mu m$ (Fig. 5.2a).

The alternating flow profiles of the microchannel with these different aspect ratios are first investigated by computational fluid dynamics (CFD) simulations (Fig. 5.2) using COMSOL Multiphysics 4.3a, a program solving partial differential equations numerically by means of the finite element method (FEM). In particular, the used mesh for the microchannels consists of more than 100'000 elements, the fluid velocities are tuned at the inlet and the incompressible Navier-Stokes equation is solved for the geometry with no-slip boundary conditions at the walls. The alteration of the flow velocity between the narrow and the wide channel regions is inverse proportional to the ratio of their width, $A_n : A_w$. Consequently, the fluid is strongly deceler-

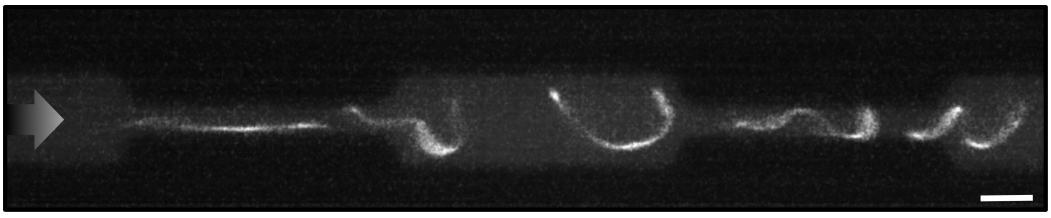

Figure 5.1: F-Actin as a model system for the non-equilibrium dynamics of individual macromolecular and biological filaments in microstructured flow. Scale bar: 5 µm. Reprinted and modified from Ref. [2].

ated while flowing from narrow to wide regions with streamlines at the exit of the narrow segment having y-components to direction of the walls whereas it is accelerated with streamlines having y-components to the direction of the center at the passage from the wide to the narrow segments (Fig. 5.2b). Here, the flow in the narrow regions has an almost parabolic flow profile, whereas a plug-like velocity profile is found in the wide regions (Fig. 5.2a).

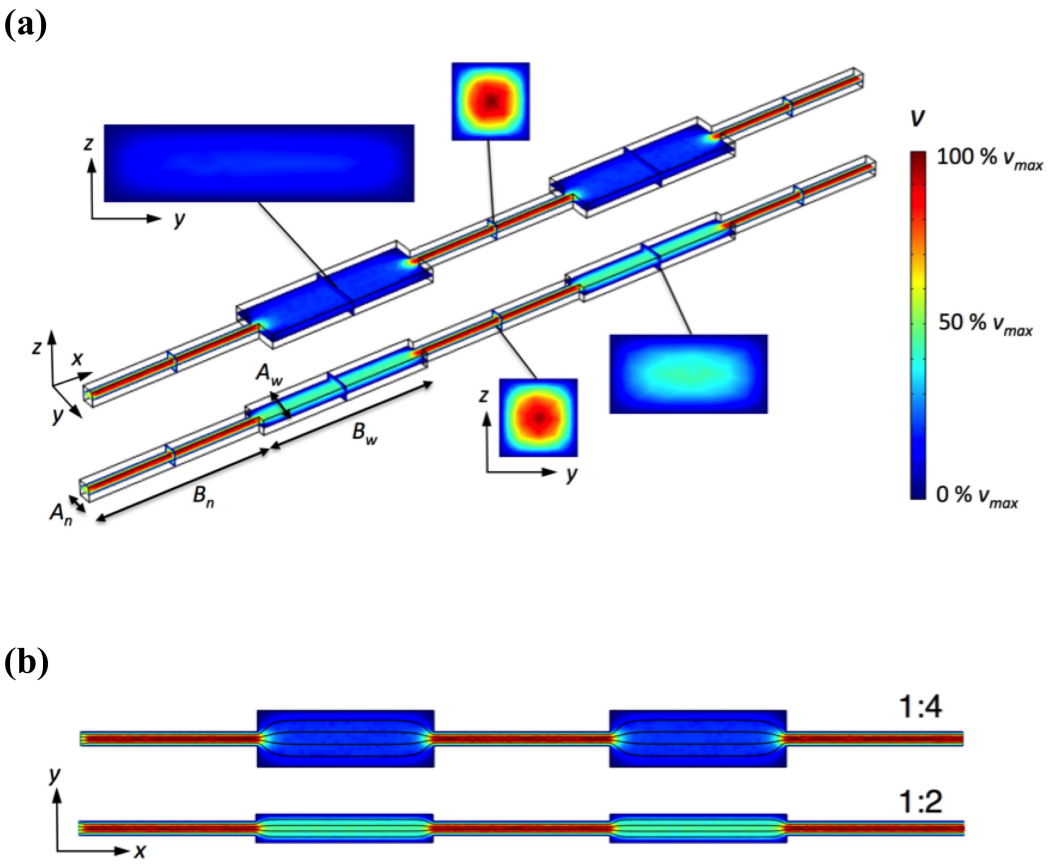

Figure 5.2: (a) CFD simulations of the (relative) velocity magnitude in channels with aspect ratios $A_n : A_w = 1 : 4$ and $A_n : A_w = 1 : 2$. The flow in the narrow regions shows an almost parabolic flow profile, whereas a plug-like velocity profile can be found in the wide regions. (b) Top (xy) view of the simulated velocity magnitude with overlaid streamlines (black lines) at the center height position ($z = 1$ µm). Reprinted and modified from Ref. [2].

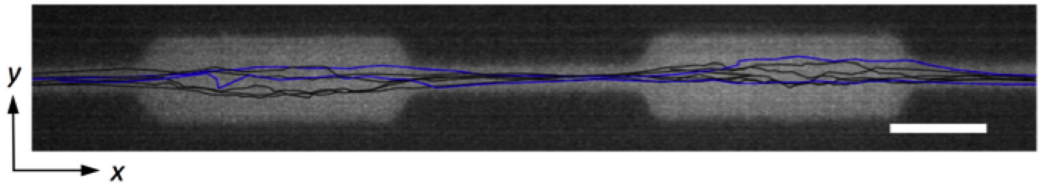

Figure 5.3: Observed center-of-mass streamlines of actin filaments with lengths of $L_c \approx 8 - 22$ µm in the channel at an aspect ratio between the narrow and the wide channel segments of 1:4. Scale bar: 10 µm. Reprinted and modified from Ref. [2].

The experimental implementation of the microfluidic design is based on soft lithography [47, 106] (experimental procedure: see appendix A). Actin filaments are observed with an Olympus IX81 inverted microscope equipped with fluorescence illumination (X-Cite Series 120 Q) and a 100 x (N.A. 1.49) UApo N oil immersion objective (Olympus, Tokyo, Japan). Images are recorded at 22 fps using a CMOS camera (pco.edge, PCO, Kelheim, Germany) with an exposure time of 45 ms and analyzed using ImageJ (version 1.47k, Wayne Rasband, National Institute of Health, USA) and MATLAB (version R2012b, The MathWorks, Natick, USA) by applying custom-developed scripts. In particular, skeleton lines of the filaments are obtained from the original fluorescence images by applying background subtraction, local contrast enhancement, Gaussian blurring and topological skeletonization using ImageJ [95,107]. These skeleton lines are used for further analysis by means of MATLAB. The center-of-mass streamlines of individual fluorecently-labelled actin filaments with lengths of $L_c \approx 8 - 22$ µm for different flow rates are shown in Fig. 5.3. Independently on their length and velocity, the centers-of-mass of flowing filaments have the tendency to follow streamlines close to the center of the microchannels, both in the narrow and wide regions.

5.3 When Symmetry Breaks Down - Evolution of Conformation and Bending Energies

Although their center-of-mass streamlines do not strongly depend on their length and velocity, actin filaments undergo strong flow-induced conformational changes while passing the microstructured device (Fig. 5.4, 5.5). In the narrow constrictions, the filaments are in an elongated, stretched conformation with low local curvatures whereas they start to buckle while entering the wider segment with the corresponding strong increase of local curvatures due to a flow-induced compression (Fig. 5.4). The nature of this compressive force can be illustrated through a moving wall model, where a semiflexible filament is pushed forward by a rigid wall, which is penetrable for the fluid and moves with a constant velocity [90].

Conversely, conformational changes of the filaments from a coiled to a stretched state occur while leaving the wider regions and reentering the nar-

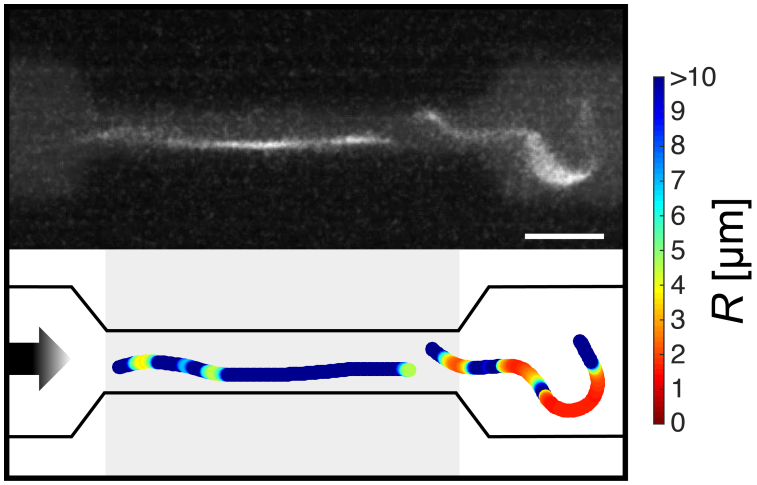

Figure 5.4: Typical flow-induced changes in the conformation of an actin filament while moving through structured microchannels. Overlay of frames from a fluorescence image sequence (top) and the corresponding local curvature (bottom) of a typical stretch-coil transition while passing from the narrow to the wide segment of the channel. Scale bar: 5 µm. Reprinted and modified from Ref. [2].

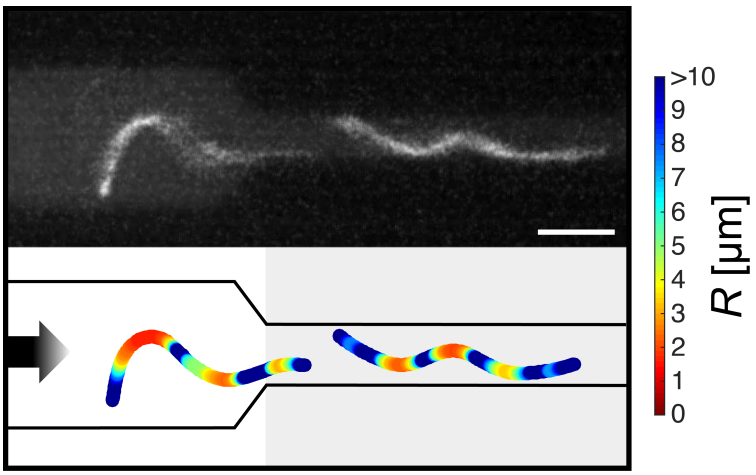

Figure 5.5: Typical flow-induced changes in the conformation of an actin filament while moving through structured microchannels. Overlay of frames from a fluorescence image sequence (top) and the corresponding local curvature (bottom) of a typical conformational transition while reentering from the wide into the narrow channel region. Scale bar: 5 µm. Reprinted and modified from Ref. [2].

row constrictions due to the acting extensional flow (Fig. 5.5). Directly at the passages from the narrow to wide regions and *vice versa*, fascinating non-equilibrium conformations can be observed: single actin filaments consisting of a stretched - low local curvatures - and a buckled - high local curvatures - part.

In order to study these stretch-coil and coil-stretch transitions, we analyzed the effect of different filament contour lengths L_c, fluid flow velocities q and microchannel aspect ratios $A_n : A_w$ on the change of the filaments' center-of-mass velocities V_{com}, end-to-end distances R_E as well as their bending energies U_b during the flow through alternating narrow and wide regions of the channel. The bending energy of the filaments are calculated from their contour lines as projections onto the image plane by [108]

$$U_b = \frac{1}{2} k_B T \cdot L_p \cdot \int_0^{L_c} R^{-2} ds \tag{5.1}$$

where k_B is the Boltzmann constant, T is the absolute temperature, L_p =10 µm is the persistence length of actin filaments [43, 109] and R are the local radii of curvatures.

5.3.1 Does Length Matter? - Grouping the Filaments According to their Contour Length

We investigated the influence of different contour lengths on the center-of-mass velocity, end-to-end distance and the bending energy of actin filaments during flow by holding the average fluid flow velocity constant at about $q = 33\,\mu m/s$ in the narrow parts of the channel. In addition, the analyzed filaments are grouped into $L_c \lesssim \frac{1}{2}L_p$ (short), $L_c \approx L_p$ (intermediate) and $L_c \approx 2L_p$ (long) according to their contour length (short: $L_c = (3.1 \pm 0.9)$ µm, intermediate: $L_c = (10.8 \pm 3.1)$ µm, long: $L_c = (19.0 \pm 3.6)$ µm). The short filaments present rigid rods, whereas the intermediate and the long filaments are described by semiflexible filaments.

The center-of-mass velocities of the filaments strongly depend on their position inside the channel, with a large decrease during the transition from

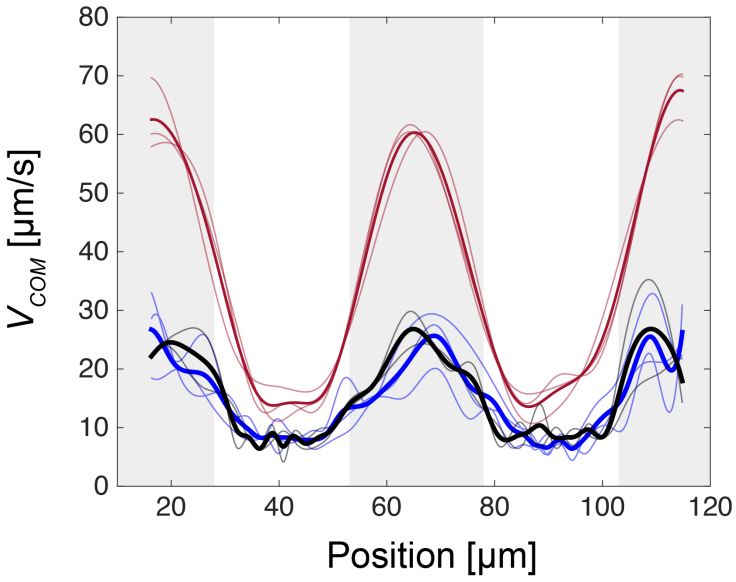

Figure 5.6: Influence of the contour length (red lines: short, black lines: intermediate, blue lines: long) on the center-of-mass velocity of actin filaments while moving through alternating narrow (grey areas) and wide regions (white areas) of the channel. The short, rigid filaments show higher center-of-mass velocities in comparison to the intermediate and long, semiflexible filaments. Reprinted and modified from Ref. [2].

the narrow ($A_n = 2$ µm) to the wide region ($A_n = 8$ µm) (Fig. 5.6). In particular, the short and rigid filaments are much faster compared to the semiflexible filaments especially in the narrow segment, whereas the center-of-mass velocities of the intermediate and long semiflexible filaments are similar and therefore showing no dependence on the contour length for filaments with $L_c \geq L_p$. During the movement from the narrow high-velocity into the wide low-velocity channel segment, the corresponding mean filament velocities decrease from $\langle v_n \rangle_{short} = (50.9 \pm 6.7)$ µm/s to $\langle v_w \rangle_{short} = (14.8 \pm 4.3)$ µm/s for rigid filaments, $\langle v_n \rangle_{im} = (21.4 \pm 4.1)$ µm/s to $\langle v_w \rangle_{im} = (9.5 \pm 2.6)$ µm/s for intermediate contour lengths and $\langle v_n \rangle_{long} = (22.1 \pm 4.1)$ µm/s to $\langle v_w \rangle_{long} = (9.1 \pm 2.1)$ µm/s for long semiflexible filaments, where $\langle v_n \rangle$ and $\langle v_w \rangle$ denote the wide and narrow regions, respectively.

Along the passage through the alternating narrow and wide low-velocity channel segments, the short and rigid filaments do not show a change of R_E with $R_E/L_c \approx 1$. Furthermore, they are preferably aligned parallel to the streamlines in the narrow channel segments and partially rotate in the wide channel regions (Fig. 5.7a). For the longer, semiflexible filaments in thermodynamic equilibrium, the end-to-end distance is given by [59, 110]

$$R_{eq} = \sqrt{\langle R_E^2 \rangle} = \sqrt{2 L_p L_c \left[1 - \frac{L_p}{L_c}\left(1 - e^{-L_c/L_p}\right)\right]} \tag{5.2}$$

resulting in a corresponding length-normalized equilibrium end-to-end distance of $(R_{eq}/L_c)_{im} = 0.85 \pm 0.03$ for the intermediate and $(R_{eq}/L_c)_{long} = 0.76 \pm 0.03$ for the long contour lengths. During the flow through the narrow channel segment, the semiflexible filaments exhibit a stretched, rod-like, non-equilibrium conformation with $R_E/L_c \approx 1$, before getting subjected to the compressive force due to the difference in fluid velocity between the narrow and wide channel segment (Fig. 5.7a). As a result, R_E/L_c decreases to a minimum of $(R_{eq}/L_c)_{long} = 0.63 \pm 0.11$ for long filaments, whereas the intermediate filaments exhibit a less pronounced decrease to $(R_{eq}/L_c)_{im} = 0.74 \pm 0.10$, which is the consequence of a larger relative stiffness L_p/L_c of intermediate filaments compared to long ones.

The length-normalized bending energies U_b/L_c are not significantly increasing for the rigid filaments, whereas the intermediate show a delayed coiling with respect to their center-of-mass position as well as a faster relaxation after the stretch-coil transition compared to long filaments (Fig. 5.7b). However, the magnitude of increase in U_b/L_c shows no difference between the intermediate and the long filaments and U_b increases from a minimum of $U_b/L_c < 0.05\,k_BT/\mu m$ for both lengths inside the narrow channel region to a maximum of $(U_b/L_c)_{long} = (0.70 \pm 0.36)\,k_BT/\mu m$ and $(U_b/L_c)_{im} = (0.84 \pm 0.37)\,k_BT/\mu m$ during flow-induced coiling.

The length-normalized end-to-end distance further indicates that the period of flow through the wide region of the channel with its plug-like flow profile is sufficient for the semiflexible filaments to already relax into a conformation of $R_E/L_c \approx R_{eq}/L_c$ (Fig. 5.7c) with a corresponding decrease in U_b/L_c (Fig. 5.7d). Subsequently, the filaments are experiencing substantial extension from R_{eq}/L_c to stretched conformations with a suppression of fluctuations at the end of the wide channel segment as well as during the passage into the narrow region.

5.3.2 Speeding Everything Up - Increasing Fluid Velocity Inside the Channel

The effect of different fluid flow velocities q on V_{com} during the flow of the filaments ($L_c = (15.7 \pm 5.4)$ µm) through the microchannel is shown in Fig. 5.8. The mean velocity of the filaments' center of mass in the narrow segment of the channel with an average fluid flow velocity of $q_{low} = 33\,\mu m/s$ was $\langle v_n \rangle_{low} = (21.9 \pm 3.7)$ µm/s, decreasing to $\langle v_w \rangle_{low} = (10.1 \pm 2.5)$ µm/s in the wide region. Increasing the average flow velocity q to $q_{high} = 108\,\mu m/s$ resulted in a large rise of $\Delta v = |\langle v_n \rangle - \langle v_w \rangle| \approx 73$ µm/s, with $\langle v_n \rangle_{high} = (113.2 \pm 29.3)$ µm/s and $\langle v_w \rangle_{high} = (40.5 \pm 14.2)$ µm/s.

The ratio of the average fluid flow velocity between the narrow (q_n) and

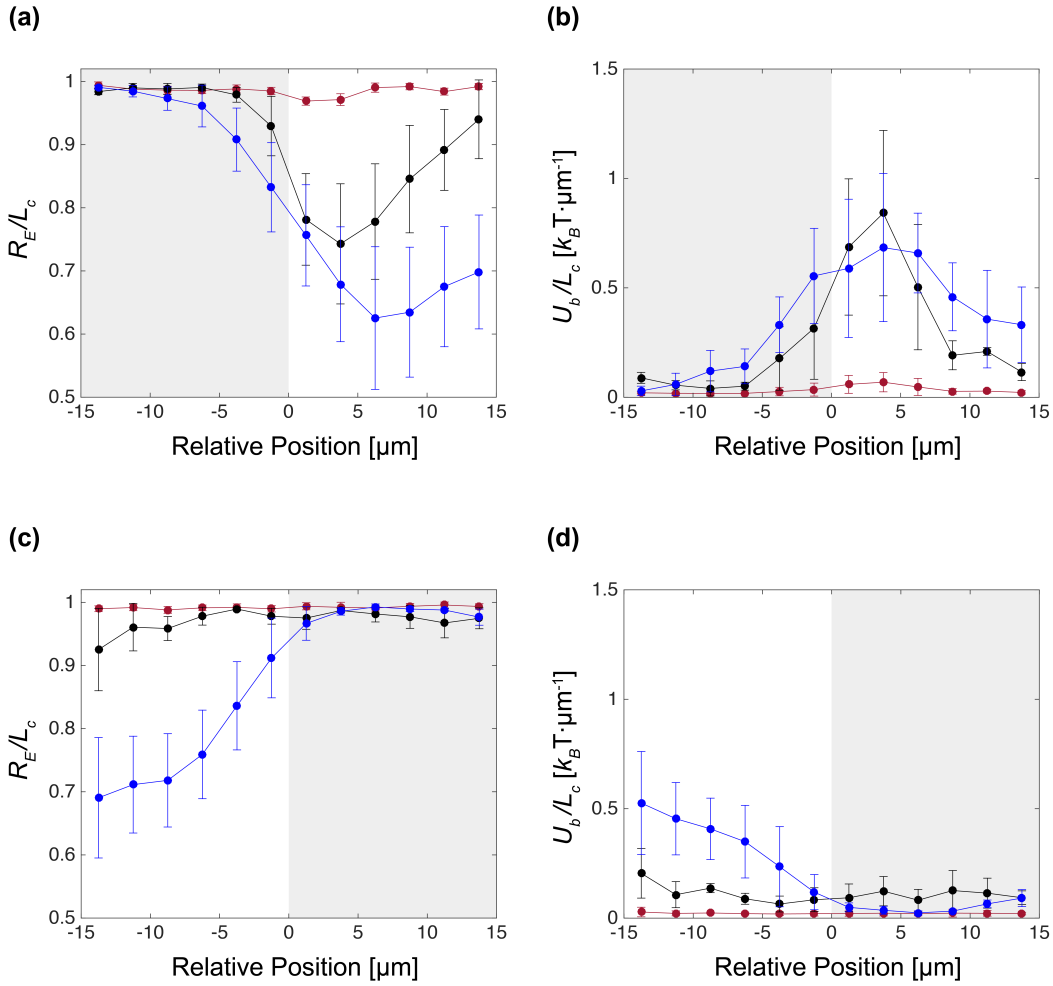

Figure 5.7: Influence of the contour length (red lines: short, black lines: intermediate, blue lines: long) on the end-to-end distance and bending energy of actin filaments while moving through alternating narrow (grey areas) and wide regions (white areas) of the channel. Evolution of the (a) end-to-end distance and the (b) length-normalized bending energy of rigid and semiflexible filaments for the movement from the narrow into the wide channel segment. Evolution of the (c) end-to-end distance and the (d) length-normalized bending energy for the movement from the wide into the narrow channel segment. Reprinted and modified from Ref. [2].

the wide (q_w) segments of the channel is $q_n/q_w = A_w/A_n = 4$, and the absolute values of the extensional or the according deceleration/compression rate

$$|\epsilon| \approx \frac{2q_n}{A_w}\left(1 - \frac{A_n}{A_w}\right) \tag{5.3}$$

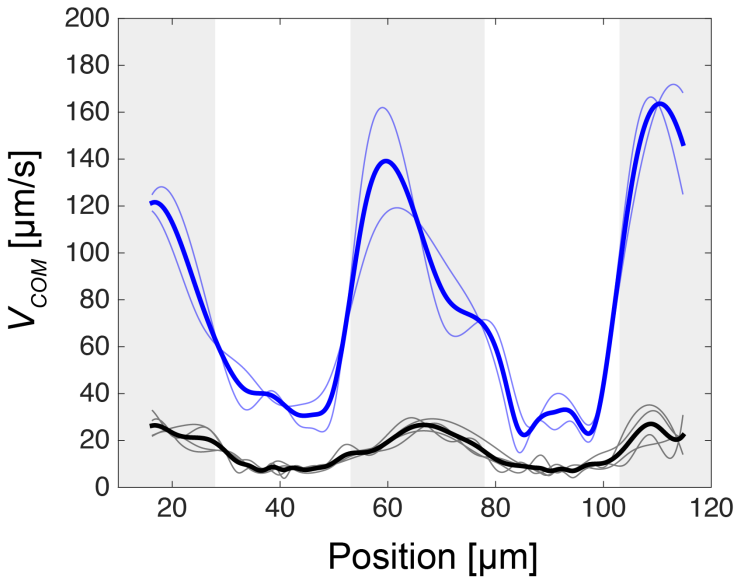

Figure 5.8: Effect of an increase in fluid flow velocity (black lines: slow, blue lines: fast) on the filaments' center-of-mass velocities while moving through alternating narrow (grey areas) and wide regions (white areas) of the channel. Increasing the fluid flow velocity leads to a higher average center-of-mass velocity as well as a larger relative difference between the channel segments. Reprinted and modified from Ref. [2].

are $|\epsilon|_{low} \approx 6\,\mathrm{s}^{-1}$ and $|\epsilon|_{high} \approx 20\,\mathrm{s}^{-1}$. However, due to the interactions of the flowing actin filaments with the different flow fields in the wide (plug flow) and the narrow channel regions (parabolic flow profile), the experimentally observed change in the center-of-mass velocities between the wide and narrow segments is smaller than the corresponding difference in average flow velocities.

Although the filaments exhibit a significantly larger rise in V_{com} and $|\epsilon|$ when exposed to a higher average flow velocity, the length-normalized end-to-end distance shows a less pronounced difference between slow and fast filaments (Fig. 5.9a). In particular, R_E/L_c decreases from a stretched conformation to a minimum of $(R_E/L_c)_{q_{low}} = 0.70 \pm 0.09$ for q_{low} and to $(R_E/L_c)_{q_{high}} = 0.63 \pm 0.08$ for fast average fluid flow velocities, respectively. In contrast, the filaments exposed to q_{high} experience a larger rise in U_b/L_c during the transition from the narrow into the wide channel segment, resulting

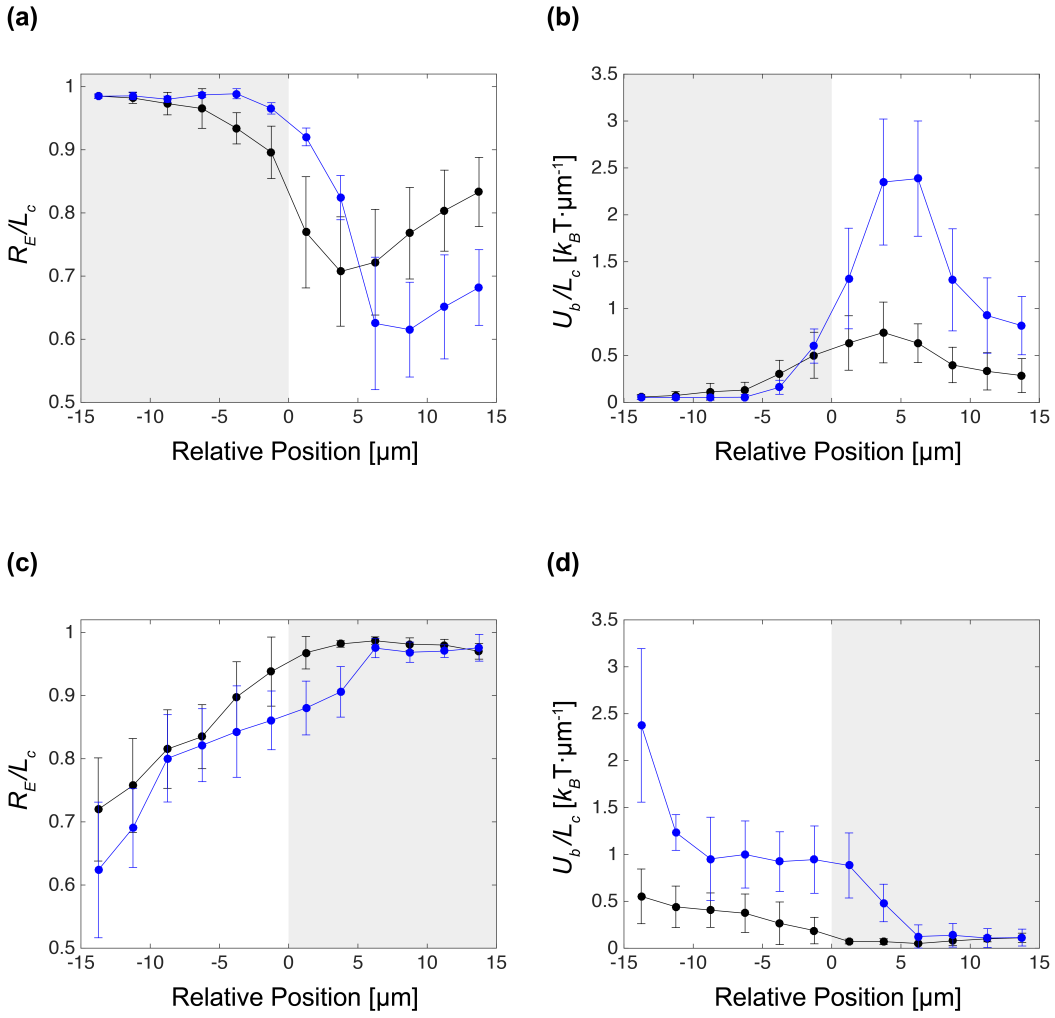

Figure 5.9: Effect of an increase in fluid flow velocity (black lines: slow, blue lines: fast) on the filaments' end-to-end distances and bending energies while moving through alternating narrow (grey areas) and wide regions (white areas) of the channel. Dependence of the (a) end-to-end distance and the (b) length-normalized bending energy on the fluid flow velocities during the stretch-coil transition. Influence of the fluid flow velocity on the (c) end-to-end distance and the (d) length-normalized bending energy of the filaments on the coil-stretch transition in extensional flow. Reprinted and modified from Ref. [2].

from the stronger spatial change in fluid flow strength and the corresponding higher compression force (Fig. 5.9b). Here, the length-normalized bending energy of the filaments increases during flow-induced coiling from a minimum

of $U_b/L_c < 0.05\,k_BT/\mu m$ within the narrow channel segment for both q to a maximum $(U_b/L_c)_{q_{low}} = (0.74 \pm 0.33)\,k_BT/\mu m$ for the low fluid flow velocity. The length-normalized bending energy of the faster filaments exhibit a higher increase to a maximum value of $(U_b/L_c)_{q_{high}} = (2.36 \pm 0.62)\,k_BT/\mu m$, which demonstrates a strong dependence of the maximum bending energy on $|\epsilon|$.

Although largely depending on the contour length, R_E/L_c shows a smaller difference between slow and fast fluid flow velocities during the filaments' flow through the wide segment of the channel and the subsequent elongation while entering the narrow channel region (Fig. 5.9c). However, with respect to rearrangement into an entirely stretched conformation before reentering the narrow channel segment, filaments exposed to a higher flow velocity are still experiencing significantly more deformation with $(R_E/L_c)_{q_{high}} = 0.86 \pm 0.04$ compared to $(R_E/L_c)_{q_{low}} = 0.94 \pm 0.05$ for filaments when applying q_{low}. Accordingly, the period of flowing through the wide region of the channel is not sufficient for filaments exposed to fast fluid flow velocities to relax into a lower bending energy conformation before reentering the narrow channel segment. In particular, filaments experiencing a high flow velocity are still exhibiting an elevated bending energy of $(U_b/L_c)_{q_{high}} = (0.96 \pm 0.36)\,k_BT/\mu m$ directly before getting elongated into the stretched conformation due to the passage into the narrow region of the microchannel (Fig. 5.9d). However, due to the relaxation into a lower bending energy conformation along the passage through the wider regions, the transition from a coiled to a stretched conformation shows no symmetry to the inverse transition (stretch-coil), although both transitions occur at the same absolute rate value $|\epsilon|$ of the fluid.

5.3.3 Narrowing it Down - Decreasing the Aspect Ratio of the Channel Segments

Decreasing the channel width of the wide segment to $A_w = 4\,\mu m$ allowed us to study the dependence of V_{com}, R_E and U_b on the aspect ratio of the microchannels and therefore on the confinement in the wider channel regions. The average fluid flow velocity is adjusted in order to obtain filaments with similar center-of-mass velocities in the region with the most pronounced coiling be-

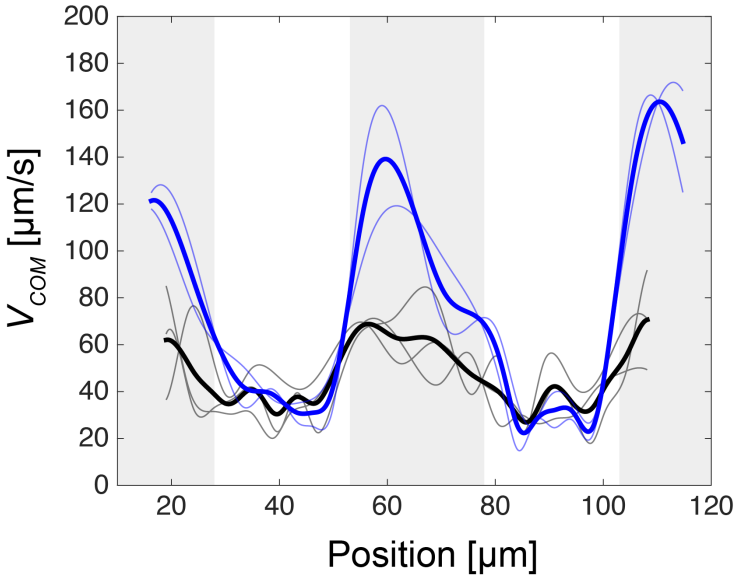

Figure 5.10: Influence of the aspect ratio between the narrow (grey areas) and wide (white areas) channel segments (black lines: 1:2, blue lines: 1:4) on the center-of-mass velocities of actin filaments while moving through the channel. Reduction of the aspect ratio causes a decrease in Δv between the distinct segments of the microchannels. Reprinted and modified from Ref. [2].

havior, i.e., the wide area of the channel. Changing the aspect ratio between the narrow and the wide segments from $A_n : A_w = 1 : 4$ to $A_n : A_w = 1 : 2$ leads to a large decrease of $\Delta v \approx 21$ µm/s, with $\langle v_n \rangle_{1:2} = (62.6 \pm 10.1)$ µm/s and $\langle v_w \rangle_{1:2} = (42.0 \pm 6.4)$ µm/s (Fig. 5.10). As a result of the smaller reduction in flow strength for the reduced aspect ratio, the magnitude of coiling while entering the low-velocity, wide channel region decreased to a less pronounced minimum in length-normalized end-to-end distance $(R_E/L_c)_{1:2} = 0.75 \pm 0.11$ in comparison to $(R_E/L_c)_{q_{1:4}} = 0.63 \pm 0.08$ (Fig. 5.11a). Correspondingly, the filaments also exhibit a smaller rise in length-normalized bending energy to a maximum of $(U_b/L_c)_{1:2} = (1.32 \pm 0.55)\, k_B T/\mu\text{m}$ in comparison to $(U_b/L_c)_{1:4} = (2.36 \pm 0.62)\, k_B T/\mu\text{m}$ (Fig. 5.11b). The end-to-end distance further effectively indicates the period of relaxation during the flow through the wide segment of the channel as well as the filaments' lateral positions during elongation into an almost straight, low-bending energy confor-

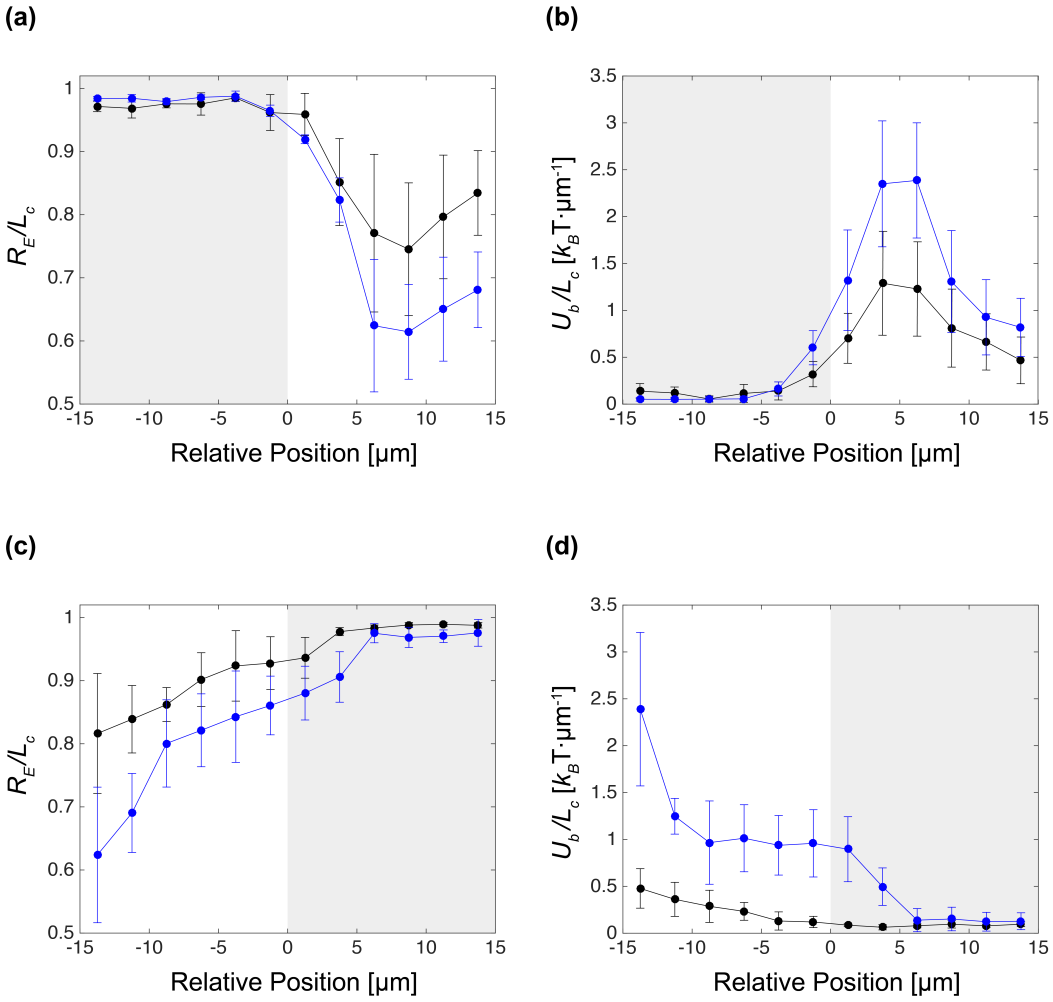

Figure 5.11: Impact of the aspect ratio between the narrow (grey areas) and wide (white areas) channel segments (black lines: 1:2, blue lines: 1:4) on the center-of-mass velocities and bending energies of actin filaments. Dependence of evolution of the (a) end-to-end distance and (b) length-normalized bending energy on the aspect ratio during the stretch-coil transition. Evolution of the (c) end-to-end distance and (d) length-normalized bending energy during the coil-stretch transition in extensional flow for different aspect ratios. Reprinted and modified from Ref. [2].

mation with $(R_E/L_c)_{1:2} = 0.93 \pm 0.04$ and $(U_b/L_c)_{1:2} = (0.10 \pm 0.06)\, k_BT/\mu m$ directly before reentering into the narrow channel region (Fig. 5.11c,d).

5.4 Bending Energies - 2D vs. 3D calculations

Due to the dynamics of our system, three-dimensional information about the filaments is not directly feasible through conventional scanning confocal microscopy. However, in order to further calculate bending curvatures from three-dimensional coordinates, we developed a straightforward approximation method of acquiring 3D positions from 2D fluorescence images (Fig. 5.12a). First, the mean intensities of pixel-value cross-sections along line segments perpendicular to the filament's two-dimensional skeleton line (Fig. 5.12b) are calculated from the processed fluorescence images. During all experiments, the objective is focused to the center of the microchannel with respect to its height, i.e., 1 µm above the cover glass surface. As a result, the maximum fluorescence intensity along a filament's skeleton line results from a position of the corresponding filament segment at $z = 1\,\mu\text{m}$, whereas a linear decrease in intensity is found from both, a filament segment leaving the focal plane to the direction of the cover glass surface at $z = 0\,\mu\text{m}$ as well as towards the top of the channel with $z = 2\,\mu\text{m}$. In order to avoid an overestimation of filament bending in z-direction, we corrected for this effect by assuming an alternating top-down sequence of filament segments with respect to maximum fluorescence intensity (Fig. 5.12c). Consequently, the corrected intensity along the filament's skeleton line is henceforth directly related to its z-coordinate. Scaling to the geometric boundaries of the channel height by assuming global intensity minima at $z = 0\,\mu\text{m}$ and maxima at $z = 2\,\mu\text{m}$ during the whole sequence of acquired images finally leads to the corresponding three-dimensional coordinates of a filament's conformation.

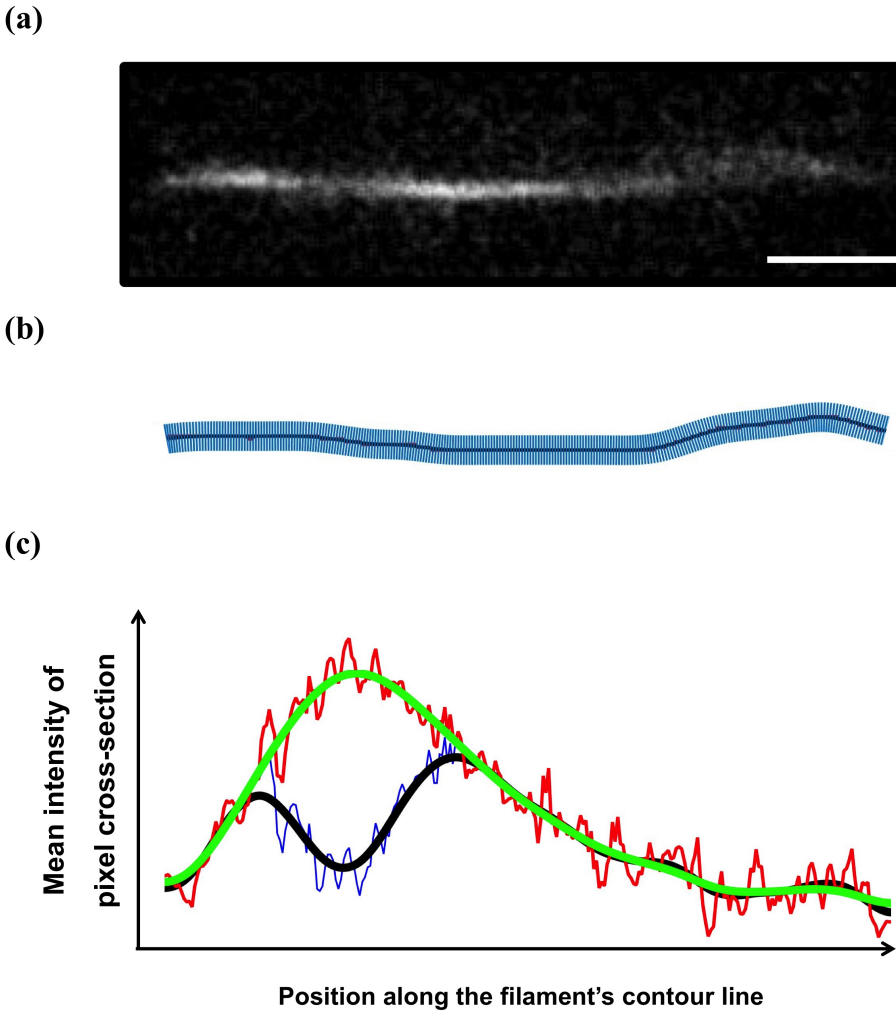

Figure 5.12: Principle of the approximation method of acquiring 3D positions from 2D fluorescence images. First, the contour of the filaments are detected from their (a) fluorescence images by applying background subtraction, local contrast enhancement, Gaussian blurring and topological skeletonization. Scale bar: 5 µm. (b) The contour line is spline-fitted (black line) and pixel cross-sections along the filament's contour are defined (blue lines). (c) The mean intensity of the pixel-cross-sections are calculated (blue line), spline-fitted (black line) and their maxima are used to correct the original intensity by assuming a alternating top-down sequence of filament segments with respect to maximum fluorescence intensity. The corrected (red line) and spline-fitted intensity (green line) of the pixel-cross-sections along the filament's contour are directly related to its position in z-direction.

A typical sequence of overlaid frames from fluorescence images and its corresponding projection onto the image plane of an actin filament flowing through several alternating segments of the microchannel are shown in Fig. 5.13a. Using our straightforward approximation method of acquiring 3D positions from 2D fluorescence images, we are able to calculate the local radii of curvature by taking into account the axial position of the filaments. However, compar-

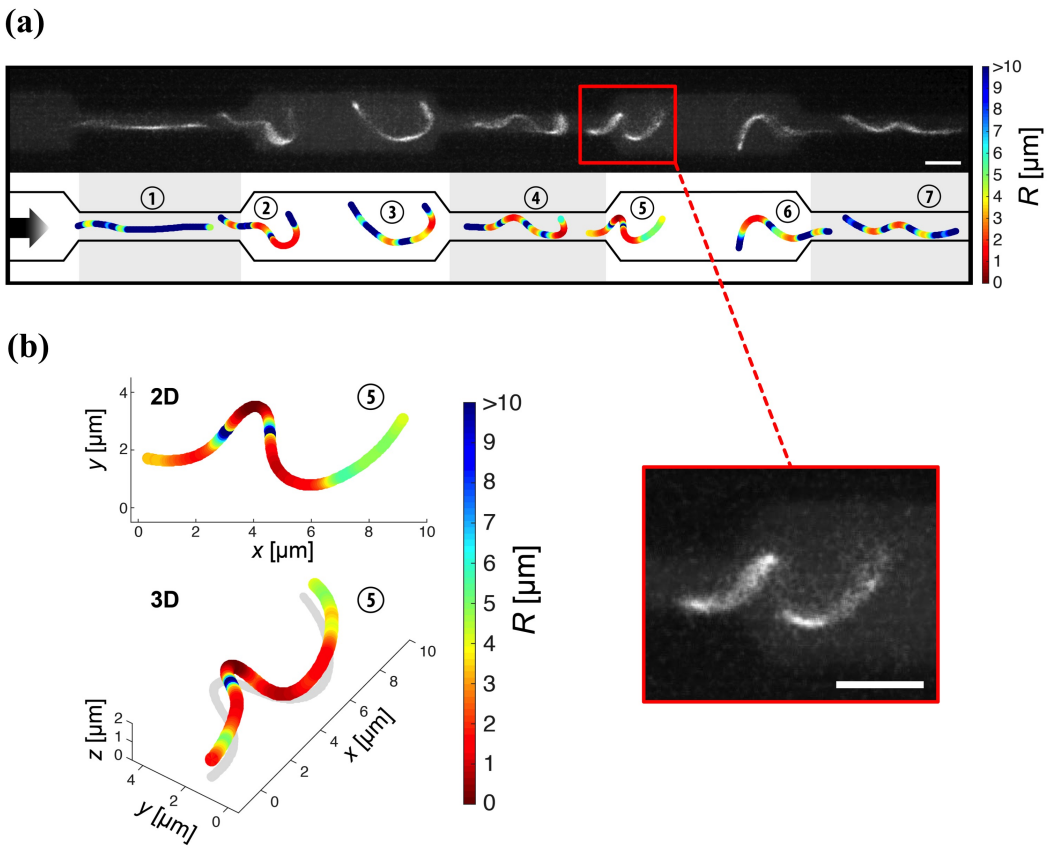

Figure 5.13: Comparison of radii of curvature obtained from *xy*-projections and from 3D coordinates with the corresponding calculated bending energy. (a) Overlay of frames from a fluorescence image sequence (top) of an actin filament and its corresponding projections onto the image *xy*-plane (bottom) while flowing through alternating segments of the microchannel. (b) Obtained radii of curvature considering solely *xy*-projections (top left) and three-dimensional reconstruction of a filament's helical conformation (right) with the obtained radii of curvature (bottom left). Scale bars: 5 µm. Reprinted and modified from Ref. [2].

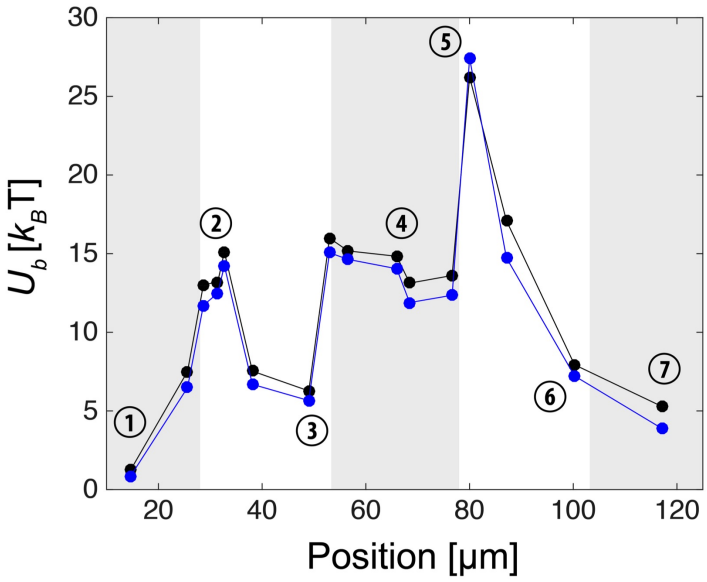

Figure 5.14: Comparison of the bending energies along the course of the moving filament (numbering corresponds to selected conformations shown in Fig. 5.13a) through alternating narrow (grey areas) and wide (white areas) segments, using the two different calculation methods (blue line: U_b from xy-projections, black line: U_b from 3D approximation). Reprinted and modified from Ref. [2].

ing these calculated radii of curvature with the radii obtained solely from the filaments' projections onto the image xy-plane, shows only minute differences (Fig. 5.13b).

In analogy to the bending energy obtained from the xy-projections, U_b is now calculated using the corresponding radii of curvature from three-dimensional coordinates. However, including the z-coordinate in the calculations results only in a marginal difference compared to solely using the radii from the filament's projections onto the image xy-plane (Fig. 5.14). This excellent agreement of the bending energies results from the chosen "pseudo"-2D microfluidic setup with a constant and low height of the microchannels having only negligible flow components in the z-direction.

Consequently, our preceding analysis by using the projection of the filaments onto the image xy-plane [111] represents an excellent and straightforward method to study the flow-induced alternating stretch-coil and coil-

stretch transitions in semiflexible actin filaments. Using the straightforward approximation method of acquiring 3D positions, we can further image a (distorted) helical coiling of the filament during hydrodynamic compression (Fig. 5.13b, "3D") as it is described in a recent simulation study [90].

Chapter 6

Conclusions[†]

In this thesis, the behavior of two different biological systems in dynamic environments is investigated by means of several methodological developments which exploit microscale physics as well as customized data and image analysis. We introduced a straightforward, self-filling microfluidic device that enables noninvasive, controlled and versatile single RBC experiments, starting directly with unprocessed human blood samples. Existing approaches to red blood cell studies typically require pre-experimental sample preparation and the principle that allows investigations specifically on the single cell level is often either based on a form of chemical fixation or active immobilization by high-intensity optical tweezers. In contrast, our method autonomously separates and isolates individual RBCs directly from the unprocessed, high cell density bulk and confines them horizontally in diffusion-controlled microchambers by solely exploiting their unique mechanical properties. The noninvasive, horizontal confinement in combination with a precise control over the RBC's microenvironment represents ideal conditions for various microscopic or spectroscopic investigations in order to quantify the temporal behavior of single RBCs exposed to an added or depleted biochemical reagent. Inside the microchambers, the motion of the RBCs is diffusive and they are therefore not experiencing adsorption-dependent changes of their intrinsic properties that can occur using chemical fixation. Due to the precise control over the RBC's environment, analysis of RBC flickering is additionally

[†]This chapter is partially reprinted and modified from Ref. [1, 2].

not limited to steady states. In particular, the dynamic measurement of non-adherent RBC's morphological response to increasing osmolarity became feasible. The time-resolved analysis of membrane edge fluctuations reveals a time delay in shape transformation of the RBC with respect to changes in osmotic concentrations. The confinement is also passive in the sense that no active immobilization by optical tweezers is needed, eliminating corresponding photo-degradation or spurious photo-induced effects that inherently prohibit the access to reversible or long-term experiments on single functional RBCs. The accumulated radiation dose introduced through high-intensity trapping lasers can lead to hemolysis of RBCs or induces the conversion of oxyHb to the inactive metHb state, both limiting the information that can be acquired by either microscopic or spectroscopic techniques. Our approach overcomes this limitation and combined with a custom-built setup for confocal resonance Raman spectroscopy we were able to record Raman spectra of functional individual RBCs purely in the oxyHb state. We showed that the laser power that is sufficient to already induce a conversion of oxyHb to deoxyHb inside the cell is in the µW range, which is only a fraction of what is typically applied in optical tweezers based methods. In summary, our specialized microfluidic device offers a unique combination of features that overcomes the limitations of available approaches and opens new possibilities for precisely controlled, reversible, long-term and time-resolved analysis of RBCs on the single-cell level. The analysis of single RBCs exposed to external stimuli will provide important insights into their fundamental biophysical properties like flickering of the membrane as well as biomedical questions regarding the disease progression in malaria or in-vitro aging of RBCs during storage in blood banks.

In the second part of this thesis, we experimentally studied the dynamics of actin filaments in spatially structured microchannels with alternating high- and low-velocity segments. A symmetric channel design is chosen with a similar absolute value of the extensional and the according deceleration/compression rate $|\epsilon|$ for the fluid flow streaming from the narrow to the wide segments and *vice versa*. Short actin filaments with a length of about $L_c \lesssim \frac{1}{2}L_p$ move as rigid rods through the structured microchannels

with a preferred parallel alignment to the streamlines in the narrow channel segments, whereas they are partially rotating in the wide channel segments. Longer, semiflexible filaments with lengths of about $L_p \lesssim L_c \lesssim 2L_p$ have a reduced center of mass velocity in comparison to the shorter rigid filaments. Moreover, the flowing semiflexible polymers mainly exhibit a buckling from a stretched, non-equilibrium conformation into a coiled conformation due to a compressive hydrodynamic force while entering into the wider channel segments. The acting compressive force leads to a strong deformation of the filaments, a reduction of the (length-normalized) end-to-end distances and storage of elastic energy due to the bending of the filaments. During this transition, the (length-normalized) end-to-end distance strongly depends on the contour length of the filament, whereas the magnitude of increase in (length-normalized) bending energy shows no evident dependence on the contour length. At lower fluid flow velocities, the period of flow through the wide channel segment is sufficient in order to relax from higher energy conformations to lower energy conformations by dissipating energy into the fluid. However, shorter semiflexible filaments relax faster into lower energy states in comparison to longer ones. At the passage from the wider channel segments to the narrow ones an extensional force is acting on the partially elastically relaxed filaments and a conformational transition from a coiled to a stretched state with a suppression of thermal fluctuations can be observed. Increasing the fluid flow velocity and therefore the extensional and the according deceleration/compression rate $|\epsilon|$ resulted in a large rise of the compressive hydrodynamic force at the passage from the narrow into the wide channel segments, which is associated with a strong increase of the bending energy of the filaments. Moreover, the periods of flow through the wide channel segments are shorter, and less relaxed filaments with higher bending energies experience an extensional flow at the passage from the wider to the narrow channel segments. Despite the symmetry of the microfluidic channels and a therefore similar rate of the fluid flow $|\epsilon|$ for compression and extension, the observed stretch-coil and coil-stretch transition distinctly differ in the evolution of the conformational changes and bending energies. The observed deviation can be attributed to the relaxation and energy dissipation of the

filaments at the passage through the wide segments. This asymmetry of the transitions is strongly dependent on the fluid flow velocity, the absolute value of the rate $|\epsilon|$ resulting from the aspect ratio $A_n : A_w$, the relaxation period being proportional to the length of wide segments B_w, the polymer length L_c, and the persistence length L_p. Summing up all these views, our presented actin studies elucidate the non-Newtonian flow behavior of semi-flexible filaments in specific microflows and therefore may have an impact on the analysis as well as sorting of polymers, which may consequently lead to a better understanding of intercellular flows.

Appendix A

Preparation of microfluidic devices for actin experiments

Silicon wafers (Si-Mat, Kaufering, Germany) were spin-coated with SU-8 2002 negative photoresist (Microchem, Newton, MA, USA) and exposed to ultraviolet light through a chromium mask (ML& C GmbH, Jena, Germany) containing the desired design. The obtained master structures were used for producing replicas in polydimethylsiloxane (PDMS, Sylgard 184, Dow Corning GmbH, Wiesbaden, Germany), which were covalently bound to a glass slide after surface activation for 30 s at 2 mbar in oxygen plasma (Harris Plasma, NY, USA). Tubings are connected to the inlet and outlet of the devices and the flow is controlled by syringe pumps (Cetoni, Korbussen, Germany). To avoid interactions of the actin filaments (experimental preparation: see appendix B) with the walls of the microchannels, the device is rinsed by a 2 mg/ml aqueous BSA (Sigma-Aldrich, Saint Louis, USA) solution for about 30 min and flushed with water. The final devices are further equilibrated in water for at least one hour before as well as during the measurements in order to prevent permeation-driven flow or an increase in buffer concentration due to the permeability properties of PDMS.

Appendix B

Preparation of actin filament solutions

Monomeric actin from rabbit skeletal muscle, fluorescently labeled Atto488-actin (protein/dye molar ratio of 1:0.6) as well as all buffers were purchased as lyophilized powders from Hypermol EK (Bielefeld, Germany) and reconstituted in water. A solution of 1 mg/ml actin contains 23.8 µM actin, 2 mM Tris-Cl (pH 8.2), 0.4 mM ATP, 0.1 mM dithiothreitol (DTT), 0.08 mM $CaCl_2$ and 0.2 % disaccharides and a solution of 23.8 µM Atto488-actin consists of 2 mM Tris-Cl (pH 8.2), 0.4 mM ATP, 0.1 mM DTT, 0.2 mM $CaCl_2$ and 0.4 % disaccharides. The monomix buffer for actin dilution contains 2 mM Tris-Cl (pH 8.2), 0.4 mM ATP, 0.1 mM $CaCl_2$ and 0.5 mM DTT, and the polymix buffer for actin polymerization consists of 1 M KCl, 0.1 M imidazole (pH 7.4), 10 mM ATP and 20 mM $MgCl_2$. In order to polymerize actin filaments, the stock solutions were mixed to a final composition of 3 µM actin (actin/Atto488-actin ratio 2:1), 1.4 mM ATP, 100 mM KCl, 2 mM $MgCl_2$, 0.09 mM $CaCl_2$, 0.4 mM DTT, 10 mM imidazole, 1.8 mM Tris-Cl (pH 7.4) and 0.05 % disaccharides. After about one hour at room temperature, actin monomers were polymerized into homogeneously labeled actin filaments and the solution was diluted at a ratio of 1:10 with a buffer mixture (monomix 90 % and polymix 10 %) in order to enable single macromolecule experiments as well as to prevent interactions among filaments [107].

Abbreviations

RBC	Red Blood Cell
Hb	Hemoglobin
PDMS	Polydimethylsiloxane
PTFE	Polytetrafluoroethylene
CMOS	Complementary Metal-Oxide-Semiconductor
PBS	Phosphate-Buffered Saline
BSA	Bovine Serum Albumin
ADE	Area-Difference-Elasticity
CCD	Charged-Coupled Device
F-Actin	Filamentous Actin
CFD	Computational Fluid Dynamics
FEM	Finite Element Method

Bibliography

[1] Göllner, M., Toma, A. C., Strelnikova, N., Deshpande, S. & Pfohl, T. A self-filling microfluidic device for noninvasive and time-resolved single red blood cell experiments. *Biomicrofluidics* **10**, 054121 (2016).

[2] Strelnikova, N., Göllner, M. & Pfohl, T. Direct observation of alternating stretch-coil and coil-stretch transitions of semiflexible polymers in microstructured flow. *Macromolecular Chemistry and Physics* **218**, 1600474 (2017).

[3] Franceschetti, D. R. *Applied Science* (Salem Press: Ipswich, 2012).

[4] Andersen, O. S. Introduction to biophysics week: What is biophysics? *Biophysical Journal* **110**, E01–E03 (2016).

[5] Popp, F.-A. & Beloussov, L. V. *Integrative Biophysics: Biophotonics* (Springer: Berling/Heidelberg, 2003).

[6] Pearson, K. *The Grammar of Science* (Walter Scott: London, 1892).

[7] Schrödinger, E. *What is Life? The Physical Aspect of the Living Cell* (Cambridge University Press: Cambridge, 1944).

[8] Assmus, H. E., Herwig, R., Cho, K.-H. & Wolkenhauer, O. Dynamics of biological systems: role of systems biology in medical research. *Expert Review of Molecular Diagnostics* **6**, 891–902 (2006).

[9] World Health Organization. *WHO Guidelines on Drawing Blood: Best Practices in Phlebotomy* (WHO Document Production Services: Geneva, 2010).

[10] Bianconi, E. *et al.* An estimation of the number of cells in the human body. *Annals of Human Biology* **40**, 463–471 (2013).

[11] Sackmann, E. *Biological Membranes Architecture and Function* (Elsevier: Amsterdam, 1995).

[12] Orians, G. H., Purves, W. K., Sadava, D. E. & Hillis, D. M. *Life: The Science of Biology.* (Sinauer Associates: Sunderland, 2011).

[13] Franco, R. S. Measurement of red cell lifespan and aging. *Transfusion Medicine and Hemotherapy* **39**, 302–307 (2012).

[14] Mohandas, N. & Gallagher, P. G. Red cell membrane: past, present, and future. *Blood* **112**, 3939–3948 (2008).

[15] Huang, S. *et al.* In vivo splenic clearance correlates with in vitro deformability of red blood cells from plasmodium yoelii-infected mice. *Infection and Immunity* **82**, 2532–2541 (2014).

[16] Cluitmans, J. C. *et al.* Alterations in red blood cell deformability during storage: a microfluidic approach. *BioMed Research International* **2014**, 764268 (2014).

[17] Browicz, T. Further observation of motion phenomena on red blood cells in pathological states. *Zentralblatt für die Medizinischen Wissenschaften* **28**, 625–627 (1890).

[18] Brochard, F. & Lennon, J. Frequency spectrum of the flicker phenomenon in erythrocytes. *Journal de Physique* **36**, 1035–1047 (1975).

[19] Strey, H., Peterson, M. & Sackmann, E. Measurement of erythrocyte membrane elasticity by flicker eigenmode decomposition. *Biophysical Journal* **69**, 478–488 (1995).

[20] Evans, J., Gratzer, W., Mohandas, N., Parker, K. & Sleep, J. Fluctuations of the red blood cell membrane: relation to mechanical properties and lack of ATP dependence. *Biophysical Journal* **94**, 4134–4144 (2008).

[21] Betz, T., Lenz, M., Joanny, J.-F. & Sykes, C. ATP-dependent mechanics of red blood cells. *Proceedings of the National Academy of Sciences* **106**, 15320–15325 (2009).

[22] Turlier, H. *et al.* Equilibrium physics breakdown reveals the active nature of red blood cell flickering. *Nature Physics* **12**, 513–519 (2016).

[23] Cojoc, D. *et al.* Toward fast malaria detection by secondary speckle sensing microscopy. *Biomedical Optics Express* **3**, 991–1005 (2012).

[24] Rey, J. *et al.* Reduced erythrocyte deformability associated with hypoargininemia during plasmodium falciparum malaria. *Scientific Reports* **4**, 3767 (2014).

[25] Evans, E. & Parsegian, V. Thermal-mechanical fluctuations enhance repulsion between bimolecular layers. *Proceedings of the National Academy of Sciences* **83**, 7132–7136 (1986).

[26] Evans, E. & Fung, Y.-C. Improved measurements of the erythrocyte geometry. *Microvascular Research* **4**, 335–347 (1972).

[27] HW, G. L., Wortis, M. & Mukhopadhyay, R. Stomatocyte–discocyte–echinocyte sequence of the human red blood cell: Evidence for the bilayer–couple hypothesis from membrane mechanics. *Proceedings of the National Academy of Sciences* **99**, 16766–16769 (2002).

[28] Melzak, K. A. *et al.* AFM measurements and lipid rearrangements: evidence from red blood cell shape changes. *Soft Matter* **8**, 7716–7726 (2012).

[29] Lázaro, G. R., Melzak, K. A., Toca-Herrera, J. L., Pagonabarraga, I. & Hernández-Machado, A. Elastic energies and morphologies of the first stages of the discoechinocyte transition. *Soft Matter* **9**, 6430–6441 (2013).

[30] Ong, C., Shen, Z., Ang, K., Kara, U. & Tang, S. Resonance Raman microspectroscopy of normal erythrocytes and plasmodium berghei-infected erythrocytes. *Applied Spectroscopy* **53**, 1097–1101 (1999).

[31] Ramser, K., Bjerneld, E. J., Fant, C., Käll, M. *et al.* Importance of substrate and photo-induced effects in Raman spectroscopy of single functional erythrocytes. *Journal of Biomedical Optics* **8**, 173–178 (2003).

[32] Ramser, K. *et al.* A microfluidic system enabling Raman measurements of the oxygenation cycle in single optically trapped red blood cells. *Lab on a Chip* **5**, 431–436 (2005).

[33] Gross, A. *et al.* Technologies for single-cell isolation. *International journal of molecular sciences* **16**, 16897–16919 (2015).

[34] Hu, P., Zhang, W., Xin, H. & Deng, G. Single cell isolation and analysis. *Frontiers in Cell and Developmental Biology* **4:216**, doi: 10.3389/fcell.2016.00116 (2016).

[35] Whitesides, G. M. The origins and the future of microfluidics. *Nature* **442**, 368–373 (2006).

[36] Purcell, E. M. Life at low reynolds number. *American Journal of Physics* **45**, 3–11 (1977).

[37] Shui, L., Eijkel, J. C. & van den Berg, A. Multiphase flow in micro- and nanochannels. *Sensors and Actuators B: Chemical* **121**, 263–276 (2007).

[38] Fainman, Y., Lee, L., Psaltis, D. & Yang, C. *Optofluidics: Fundamentals, Devices, and Applications* (McGraw-Hill: New York, 2009).

[39] Schuster, H. G. & Grigoriev, R. *Transport and Mixing in Laminar Flows: From Microfluidics to Oceanic Currents* (John Wiley & Sons: Hoboken, 2012).

[40] Reynolds, O. An experimental investigation of the circumstances which determine whether the motion of water shall be direct or sinuous, and of the law of resistance in parallel channels. *Philosophical Transactions of the Royal Society of London* **174**, 935–982 (1883).

[41] Squires, T. M. & Quake, S. R. Microfluidics: Fluid physics at the nanoliter scale. *Reviews of Modern Physics* **77**, 977 (2005).

[42] Deshpande, S. & Pfohl, T. Hierarchical self-assembly of actin in microconfinements using microfluidics. *Biomicrofluidics* **6**, 034120 (2012).

[43] Deshpande, S. & Pfohl, T. Real-time dynamics of emerging actin networks in cell-mimicking compartments. *PloS One* **10**, e0116521 (2015).

[44] Hochstetter, A. *et al.* Microfluidics-based single cell analysis reveals drug-dependent motility changes in trypanosomes. *Lab on a Chip* **15**, 1961–1968 (2015).

[45] Vitagliano, V. & Lyons, P. Diffusion coefficients for aqueous solutions of sodium chloride and barium chloride. *Journal of the American Chemical Society* **78**, 1549–1552 (1956).

[46] Hamer, W. J. & Wu, Y.-C. Osmotic coefficients and mean activity coefficients of uni-univalent electrolytes in water at 25°C. *Journal of Physical and Chemical Reference Data* **1**, 1047–1100 (1972).

[47] Xia, Y. & Whitesides, G. M. Soft lithography. *Annual Review of Materials Science* **28**, 153–184 (1998).

[48] Whitesides, G. M. & Stroock, A. D. Flexible methods for microfluidics. *Phyics Today* **54**, 42–48 (2001).

[49] McDonald, J. C. & Whitesides, G. M. Poly(dimethylsiloxane) as a material for fabricating microfluidic devices. *Accounts of Chemical Research* **35**, 491–499 (2002).

[50] Beh, C. W., Zhou, W. & Wang, T.-H. Pdms–glass bonding using grafted polymeric adhesive–alternative process flow for compatibility with patterned biological molecules. *Lab on a Chip* **12**, 4120–4127 (2012).

[51] Weibel, D. B., DiLuzio, W. R. & Whitesides, G. M. Microfabrication meets microbiology. *Nature Reviews Microbiology* **5**, 209–218 (2007).

[52] Bhattacharya, S., Datta, A., Berg, J. M. & Gangopadhyay, S. Studies on surface wettability of poly(dimethyl)siloxane (PDMS) and glass under oxygen-plasma treatment and correlation with bond strength. *Journal of Microelectromechanical Systems* **14**, 590–597 (2005).

[53] Jo, B.-H., Van Lerberghe, L. M., Motsegood, K. M. & Beebe, D. J. Three-dimensional micro-channel fabrication in polydimethylsiloxane (PDMS) elastomer. *Journal of Microelectromechanical Systems* **9**, 76–81 (2000).

[54] Kim, J., Chaudhury, M. K. & Owen, M. J. Hydrophobic recovery of polydimethylsiloxane elastomer exposed to partial electrical discharge. *Journal of Colloid and Interface Science* **226**, 231–236 (2000).

[55] Kim, J., Chaudhury, M. K., Owen, M. J. & Orbeck, T. The mechanisms of hydrophobic recovery of polydimethylsiloxane elastomers exposed to partial electrical discharges. *Journal of Colloid and Interface Science* **244**, 200–207 (2001).

[56] Lee, J. N., Park, C. & Whitesides, G. M. Solvent compatibility of poly (dimethylsiloxane)-based microfluidic devices. *Analytical Chemistry* **75**, 6544–6554 (2003).

[57] Eddington, D. T., Puccinelli, J. P. & Beebe, D. J. Thermal aging and reduced hydrophobic recovery of polydimethylsiloxane. *Sensors and Actuators B: Chemical* **114**, 170–172 (2006).

[58] Hoffman, J. F. On red blood cells, hemolysis and resealed ghosts. In *The Use of Resealed Erythrocytes as Carriers and Bioreactors*, 1–15 (Springer: New York, 1992).

[59] Uppaluri, S. *et al.* Impact of microscopic motility on the swimming behavior of parasites: straighter trypanosomes are more directional. *PLoS Computational Biology* **7**, e1002058 (2011).

[60] Han, Y. *et al.* Brownian motion of an ellipsoid. *Science* **314**, 626–630 (2006).

[61] Ehrlich, R. & Weinberg, B. An exact method for characterization of grain shape. *Journal of Sedimentary Research* **40**, 205–212 (1970).

[62] MacLeod, N. Semilandmarks and radial fourier analysis. *Palaeontology Newletter* **76**, 25–42 (2011).

[63] Johnson, W. C. *Mathematical and Physical Principles of Engineering Analysis* (McGraw-Hill: New York, 1944).

[64] Helfrich, W. Elastic properties of lipid bilayers: theory and possible experiments. *Zeitschrift für Naturforschung C* **28**, 693–703 (1973).

[65] Sheetz, M. P. & Singer, S. Biological membranes as bilayer couples. a molecular mechanism of drug-erythrocyte interactions. *Proceedings of the National Academy of Sciences* **71**, 4457–4461 (1974).

[66] Miao, L., Seifert, U., Wortis, M. & Döbereiner, H.-G. Budding transitions of fluid-bilayer vesicles: the effect of area-difference elasticity. *Physical Review E* **49**, 5389 (1994).

[67] Iglič, A. A possible mechanism determining the stability of spiculated red blood cells. *Journal of Biomechanics* **30**, 35–40 (1997).

[68] Khairy, K. & Howard, J. Minimum-energy vesicle and cell shapes calculated using spherical harmonics parameterization. *Soft Matter* **7**, 2138–2143 (2011).

[69] Gianolio, E., Ferrauto, G., Di Gregorio, E. & Aime, S. Re-evaluation of the water exchange lifetime value across red blood cell membrane. *Biochimica et Biophysica Acta - Biomembranes* **1858**, 627–631 (2016).

[70] Tuvia, S. *et al.* Cell membrane fluctuations are regulated by medium macroviscosity: evidence for a metabolic driving force. *Proceedings of the National Academy of Sciences* **94**, 5045–5049 (1997).

[71] Wood, B. R. & McNaughton, D. Micro-Raman characterization of high- and low-spin heme moieties within single living erythrocytes. *Biopolymers* **67**, 259–262 (2002).

[72] Xie, C. & Li, Y.-Q. Confocal micro-Raman spectroscopy of single biological cells using optical trapping and shifted excitation difference techniques. *Journal of Applied Physics* **93**, 2982–2986 (2003).

[73] Wood, B. R., Caspers, P., Puppels, G. J., Pandiancherri, S. & McNaughton, D. Resonance Raman spectroscopy of red blood cells using near-infrared laser excitation. *Analytical and Bioanalytical Chemistry* **387**, 1691–1703 (2007).

[74] De Luca, A. C. *et al.* Spectroscopical and mechanical characterization of normal and thalassemic red blood cells by Raman tweezers. *Optics Express* **16**, 7943–7957 (2008).

[75] Rusciano, G., Pesce, G. & Sasso, A. Resonance Raman spectroscopy and mechanics of single red blood cell manipulated by optical tweezers. *Haematologica* **92**, 174–183 (2007).

[76] Rusciano, G., De Luca, A. C., Pesce, G. & Sasso, A. Raman tweezers as a diagnostic tool of hemoglobin-related blood disorders. *Sensors* **8**, 7818–7832 (2008).

[77] Bowley, H. J. *et al.* *Practical Raman Spectroscopy* (Springer: Berlin/Heidelberg, 2012).

[78] Efremov, E. V., Ariese, F. & Gooijer, C. Achievements in resonance Raman spectroscopy: Review of a technique with a distinct analytical chemistry potential. *Analytica Chimica Acta* **606**, 119–134 (2008).

[79] Smith, E. & Dent, G. *Modern Raman Spectroscopy - A Practical Approach* (John Wiley & Sons: Hoboken, 2005).

[80] Ramser, K. *et al.* Resonance Raman spectroscopy of optically trapped functional erythrocytes. *Journal of Biomedical Optics* **9**, 593–600 (2004).

[81] Strekas, T. C. & Spiro, T. G. Hemoglobin: resonance Raman spectra. *Biochimica et Biophysica Acta - Protein Structure* **263**, 830–833 (1972).

[82] Brunner, H. & Sussner, H. Resonance Raman scattering on haemoglobin. *Biochimica et Biophysica Acta - Protein Structure* **310**, 20–31 (1973).

[83] Bankapur, A., Zachariah, E., Chidangil, S., Valiathan, M. & Mathur, D. Raman tweezers spectroscopy of live, single red and white blood cells. *PLoS One* **5**, e10427 (2010).

[84] Pollard, T. D. & Cooper, J. A. Actin and actin-binding proteins. a critical evaluation of mechanisms and functions. *Annual Review of Biochemistry* **55**, 987–1035 (1986).

[85] Lodish, H. *Molecular Cell Biology* (Macmillan: London, 2008).

[86] Agre, P. *Red Blood Cell Membranes: Structure, Function, Clinical Implications* (CRC Press: Boca Raton, 1989).

[87] Le Goff, L., Hallatschek, O., Frey, E. & Amblard, F. Tracer studies on F-actin fluctuations. *Physical Review Letters* **89**, 258101 (2002).

[88] Ott, A., Magnasco, M., Simon, A. & Libchaber, A. Measurement of the persistence length of polymerized actin using fluorescence microscopy. *Physical Review E* **48**, R1642 (1993).

[89] Pfohl, T., Mugele, F., Seemann, R. & Herminghaus, S. Trends in microfluidics with complex fluids. *ChemPhysChem* **4**, 1291–1298 (2003).

[90] Chelakkot, R., Winkler, R. G. & Gompper, G. Flow-induced helical coiling of semiflexible polymers in structured microchannels. *Physical Review Letters* **109**, 178101 (2012).

[91] Kantsler, V. & Goldstein, R. E. Fluctuations, dynamics, and the stretch-coil transition of single actin filaments in extensional flows. *Physical Review Letters* **108**, 038103 (2012).

[92] Young, Y.-N. & Shelley, M. J. Stretch-coil transition and transport of fibers in cellular flows. *Physical Review Letters* **99**, 058303 (2007).

[93] Manikantan, H. & Saintillan, D. Buckling transition of a semiflexible filament in extensional flow. *Physical Review E* **92**, 041002 (2015).

[94] Golubovic, L., Moldovan, D. & Peredera, A. Flexible polymers and thin rods far from equilibrium: buckling dynamics. *Physical Review E* **61**, 1703 (2000).

[95] Steinhauser, D., Köster, S. & Pfohl, T. Mobility gradient induces cross-streamline migration of semiflexible polymers. *ACS Macro Letters* **1**, 541–545 (2012).

[96] Harasim, M., Wunderlich, B., Peleg, O., Kröger, M. & Bausch, A. R. Direct observation of the dynamics of semiflexible polymers in shear flow. *Physical Review Letters* **110**, 108302 (2013).

[97] Guglielmini, L., Kushwaha, A., Shaqfeh, E. S. & Stone, H. A. Buckling transitions of an elastic filament in a viscous stagnation point flow. *Physics of Fluids* **24**, 123601 (2012).

[98] Levy, S. L. & Craighead, H. G. DNA manipulation, sorting, and mapping in nanofluidic systems. *Chemical Society Reviews* **39**, 1133–1152 (2010).

[99] Kirchenbuechler, I., Guu, D., Kurniawan, N. A., Koenderink, G. H. & Lettinga, M. P. Direct visualization of flow-induced conformational transitions of single actin filaments in entangled solutions. *Nature Communications* **5**, 5060 (2014).

[100] Huber, B., Harasim, M., Wunderlich, B., Kröger, M. & Bausch, A. R. Microscopic origin of the non-newtonian viscosity of semiflexible polymer solutions in the semidilute regime. *ACS Macro Letters* **3**, 136–140 (2014).

[101] Manikantan, H. & Saintillan, D. Subdiffusive transport of fluctuating elastic filaments in cellular flows. *Physics of Fluids* **25**, 073603 (2013).

[102] Woodhouse, F. G. & Goldstein, R. E. Cytoplasmic streaming in plant cells emerges naturally by microfilament self-organization. *Proceedings of the National Academy of Sciences* **110**, 14132–14137 (2013).

[103] Tominaga, M. & Ito, K. The molecular mechanism and physiological role of cytoplasmic streaming. *Current Opinion in Plant Biology* **27**, 104 – 110 (2015).

[104] Verchot-Lubicz, J. & Goldstein, R. E. Cytoplasmic streaming enables the distribution of molecules and vesicles in large plant cells. *Protoplasma* **240**, 99–107 (2010).

[105] De Groot, S. R. & Mazur, P. *Non-Equilibrium Thermodynamics* (Dover: New York, 1984).

[106] Köster, S. & Pfohl, T. An in vitro model system for cytoskeletal confinement. *Cell Motility and the Cytoskeleton* **66**, 771–776 (2009).

[107] Köster, S., Steinhauser, D. & Pfohl, T. Brownian motion of actin filaments in confining microchannels. *Journal of Physics: Condensed Matter* **17**, S4091 (2005).

[108] Powers, T. R. Dynamics of filaments and membranes in a viscous fluid. *Reviews of Modern Physics* **82**, 1607 (2010).

[109] Wen, Q. & Janmey, P. A. Polymer physics of the cytoskeleton. *Current Opinion in Solid State and Materials Science* **15**, 177–182 (2011).

[110] Colby, R. & Rubinstein, M. *Polymer Physics* (Oxford University Press: Oxford, 2003).

[111] Nöding, B. & Köster, S. Intermediate filaments in small configuration spaces. *Physical Review Letters* **108**, 088101 (2012).

Publications

M. Göllner, A. C. Toma, N. Strelnikova, S. Deshpande and T. Pfohl. A self-filling microfluidic device for noninvasive and time-resolved single red blood cell experiments. *Biomicrofluidics* **10**, 054121 (2016)

N. Strelnikova*, M.Göllner* and T. Pfohl. Direct observation of alternating stretch-coil and coil-stretch transitions of semiflexible polymers in microstructured flow. *Macromolecular Chemistry and Physics* **218**, 1600474 (2017) *contributed equally

N. Strelnikova, N. Sauter, M. Guizar-Sicairos, M. Göllner, A. Diaz, P. Delivani, M. Chacon, I. Tolic-Norrelykke, V. Zaburdaev and T. Pfohl. Live cell X-ray imaging of autophagic vacuoles formation and chromatin dynamics in fission yeast. (under review)

Acknowledgements

The last four years have been a great time for me and I am very grateful for that. First and foremost, I would like to thank my supervisor **Thomas Pfohl** for the opportunity to do this interesting PhD in his research group and the support throughout the duration of this work. Especially the latter was really important to me and I appreciate all the discussions. Most importantly, the certainty of him having always an open ear for people's problems - scientific and personal - made it a truly special working atmosphere. During my time as one of his PhD students, I have not only learned a lot with respect to specific scientific challenges but also how to approach and understand science in general as well as how to follow and to stand up for the own scientific convictions. We further had amazing and unique group trips where highlights for me have been for sure the snow shoe hike in the Swiss mountains and the group hike to the Rothaus brewery including the controlled way of getting lost in the forest as well as the alcohol-free beer... Furthermore, I really enjoyed all the smaller activities we had together as a group, like the very nice Christmas dinners and celebrations after work. Especially the non-PhD-related research with respect to challenging the limits of human physiology by well-thought(!) fast food experiments will remain unforgotten moments.

Moreover, I would like to thank **Cornelia Palivan** for being the co-referee for my thesis and especially for integrating me into her group during the last year of my PhD. Although I came from a different group and scientific direction, I always felt welcome to ask for her help with scientific, administrative and personal issues. During this time I had contact to several of her students that have been very friendly, helpful and further gave interesting input into my projects during the seminars. I also want to thank **Wolfgang Meier**

for acting as the faculty representative for my thesis as well as for the kind integration into his group.

A special thanks goes to my colleagues **Natalja, Michael, Nora, Cora, Axel, Raphael, Siddharth and Adriana**. During all the group activities we had a lot of fun and although we didn't always agree on everything, I appreciate all the moments with them. Especially Adriana helped me a lot during the first months of my PhD by introducing me into my project, microfluidics as well as all the necessary fabrication processes. I further did not experience a competitive atmosphere and could always ask all of them for their unselfish support. Some of my colleagues further became very good friends of mine during the last four years and I am looking forward to all the great moments we will share in the future! Last but not least, I thank all my friends and my family for constant encouragement, love and support.